The Astrophysical Journal, 857:130 (16pp), 2018 April 20 https://doi.org/10.3847/1538-4357/aab709

Numerical Simulation of Coronal Waves Interacting with Coronal Holes. II. Dependence on Alfvén Speed Inside the Coronal Hole

Isabell Piantschitsch[1], Bojan Vršnak[2], Arnold Hanslmeier[1], Birgit Lemmerer[1], Astrid Veronig[1], Aaron Hernandez-Perez[1], and Jaša Čalogović[2]
[1] IGAM/Institute of Physics, University of Graz, Universitätsplatz 5, A-8010 Graz, Austria; isabell.piantschitsch@uni-graz.at
[2] Hvar Observatory, Faculty of Geodesy, Kačićeva 26, HR-10000 Zagreb, Croatia
Received 2017 September 12; revised 2018 February 22; accepted 2018 March 2; published 2018 April 24

Abstract

We used our newly developed magnetohydrodynamic (MHD) code to perform 2.5D simulations of a fast-mode MHD wave interacting with coronal holes (CHs) of varying Alfvén speed that result from assuming different CH densities. We find that this interaction leads to effects like reflection, transmission, stationary fronts at the CH boundary, and the formation of a density depletion that moves in the opposite direction to the incoming wave. We compare these effects with regard to the different CH densities and present a comprehensive analysis of morphology and kinematics of the associated secondary waves. We find that the density value inside the CH influences the phase speed and the amplitude values of density and magnetic field for all different secondary waves. Moreover, we observe a correlation between the CH density and the peak values of the stationary fronts at the CH boundary. The findings of reflection and transmission on the one hand and the formation of stationary fronts caused by the interaction of MHD waves with CHs on the other hand strongly support the theory that large-scale disturbances in the corona are fast-mode MHD waves.

Key words: magnetohydrodynamics (MHD) – Sun: corona – Sun: evolution – waves

Supporting material: animation

1. Introduction

Large-scale propagating disturbances in the corona, or coronal waves, as they are also called, were directly observed for the first time by the Extreme-ultraviolet Imaging Telescope (EIT; Delaboudinière et al. 1995) on board the *Solar and Heliospheric Observatory* (Domingo et al. 1995). They are driven by solar flares or alternatively by coronal mass ejections (CMEs; for a comprehensive review see, e.g., Vršnak & Cliver 2008) and can be observed over the entire solar surface.

Inconsistencies regarding the analysis and comparison of observations and simulations led to the development of different theories on how to interpret coronal waves (Long et al. 2017). Coronal waves can be described by wave theories, which consider the disturbances as fast-mode MHD waves (Thompson et al. 1998; Vršnak & Lulić 2000; Wang 2000; Wu et al. 2001; Ofman & Thompson 2002; Warmuth et al. 2004; Patsourakos & Vourlidas 2009; Patsourakos et al. 2009; Schmidt & Ofman 2010; Veronig et al. 2010; Lulić & Vršnak 2013). Alternatively, coronal waves can be explained by so-called pseudo-wave theories, which consider the observed disturbances as a result of the reconfiguration of the coronal magnetic field, caused by continuous small-scale reconnection (Attrill et al. 2007a, 2007b; van Driel-Gesztelyi et al. 2008), Joule heating (Delannée et al. 2007), or stretching of magnetic field lines (Chen et al. 2002). Effects like reflection, refraction, or transmission of coronal waves at a coronal hole (CH) boundary support the wave theory, whereas the existence of stationary bright fronts was one of the primary reasons for the development of the competing pseudo-wave theory. Another alternative approach is hybrid models that try to combine both wave and pseudo-wave theories by interpreting the outer envelope of a CME as a pseudo-wave that is followed by a freely propagating fast-mode MHD wave (Chen et al. 2002, 2005; Zhukov & Auchère 2004; Cohen et al. 2009; Liu et al. 2010; Chen & Wu 2011; Downs et al. 2011; Cheng et al. 2012). Recent observations also include both the wave and nonwave approach in the interpretation of an individual EUV wave event (Zong & Dai 2017).

However, among these competing theories, the wave interpretation is regarded as the best-supported approach (Warmuth 2015; Long et al. 2017). Observational evidence for the wave character of these large-scale propagating disturbances is given by various authors who report about waves being reflected and refracted at a CH (Long et al. 2008; Veronig et al. 2008; Gopalswamy et al. 2009; Kienreich et al. 2013), or waves being transmitted through a CH (Olmedo et al. 2012), or EIT wave fronts pushing plasma downward (Harra et al. 2011; Veronig et al. 2011), which is also consistent with the interpretation that EIT waves are fast-mode MHD waves. Recent observations also show that fast EUV waves are able to form bright stationary fronts at the boundary of a magnetic separatrix layer (Chandra et al. 2016). Furthermore, studies on simulating coronal waves indicate that stationary wave fronts at a CH boundary can be produced by the interaction of a fast-mode MHD wave with obstacles like a CH (Piantschitsch et al. 2017) or a magnetic quasi-separatrix layer (Chen et al. 2016) and therefore confirm the above-mentioned observations.

In Piantschitsch et al. (2017) we used a newly developed MHD code to perform 2.5D simulations, which showed that the interaction of an MHD wave with a low-density region like a CH leads to effects like reflection and transmission of the incoming wave. Moreover, we observed stationary features at the CH boundary and the formation of a density depletion that is moving in the opposite direction of the incoming wave propagation. We found reflections inside the CH that subsequently led to additional transmissive and reflective features outside the CH. We showed that the incoming wave pushes the

CH boundary in the direction of wave propagation. Additionally, we compared phase speeds and positions of the incoming wave and the resulting waves after the interaction with a CH and found good agreement with observational cases where waves were being reflected and refracted at a CH (Kienreich et al. 2013) or transmitted through a CH (Olmedo et al. 2012).

In Piantschitsch et al. (2017) we assumed a certain initial density amplitude for the incoming wave and a fixed CH density for our simulations. In this paper we focus on the comparison of different CH densities and on how these various densities change the kinematics of the secondary waves (i.e., reflected, transmitted, and traversing waves) and the stationary features at the CH boundary. These different CH densities lead subsequently to different Alfvén speeds inside the CH. We will show that there is an influence of the CH density and the Alfvén speed, respectively, on the amplitude values of the secondary waves and the peak values of the stationary features.

In Section 2 we describe the initial conditions and present the numerical method we use for our simulations. A comprehensive description of the morphology of the reflected, traversing, and transmitted waves will be presented in Section 3. In Section 4 we analyze the kinematic measurements of secondary waves and stationary features and compare the cases of varying CH densities. In Sections 5 and 6 we discuss the conclusions that can be drawn from our simulation results.

2. Numerical Setup

2.1. Algorithm and Equations

We use our newly developed code to perform 2.5D simulations of MHD wave propagation and its interaction with low-density regions of varying density. In this code we numerically solve the standard homogeneous MHD equations (for detailed description of the equations see Piantschitsch et al. 2017) by applying the so-called Total Variation Diminishing Lax–Friedrichs scheme, first described by Tóth & Odstrčil (1996). This scheme is a fully explicit method and achieves second-order accuracy in space and time. The simulations are performed by using a 500×300 resolution and a dimensionless length of the computational box equal to 1.0 in both the x- and y-direction. Transmissive boundary conditions are used for the simulation boundaries.

2.2. Initial Conditions

We assume an idealized case with zero pressure all over the computational box and a homogeneous magnetic field in the vertical direction. The initial setup describes five different cases for the density distribution inside the CH, starting from a density value of $\rho_{\mathrm{CH}} = 0.1$ and going up to $\rho_{\mathrm{CH}} = 0.5$. The detailed initial conditions for all parameters are as follows:

$$\rho(x) = \begin{cases} \Delta\rho \cdot \cos^2\left(\pi \dfrac{x - x_0}{\Delta x}\right) + \rho_0 & 0.05 \leqslant x \leqslant 0.15 \\ 0.1 \vee 0.2 \vee 0.3 \vee 0.4 \vee 0.5 & 0.4 \leqslant x \leqslant 0.6 \\ 1.0 & \text{else} \end{cases}, \quad (1)$$

$$v_x(x) = \begin{cases} 2 \cdot \sqrt{\dfrac{\rho(x)}{\rho_0}} - 2.0 & 0.05 \leqslant x \leqslant 0.15 \\ 0 & \text{else} \end{cases}, \quad (2)$$

$$B_z(x) = \begin{cases} \rho(x) & 0.05 \leqslant x \leqslant 0.15 \\ 1.0 & \text{else} \end{cases}, \quad (3)$$

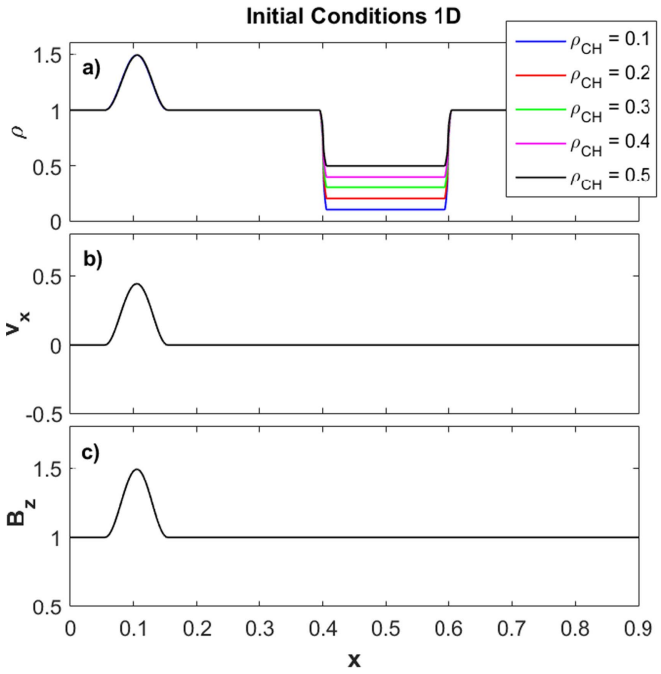

Figure 1. Initial conditions for density ρ, plasma flow velocity v_x, and magnetic field in z-direction B_z for five different densities inside the CH, starting from $\rho_{\mathrm{CH}} = 0.1$ (blue solid line), increasing by steps of 0.1, and ending with $\rho_{\mathrm{CH}} = 0.5$ (black solid line in the range $0.4 \leqslant x \leqslant 0.6$).

$$B_x = B_y = 0, \qquad 0 \leqslant x \leqslant 1, \quad (4)$$

$$v_y = v_z = 0, \qquad 0 \leqslant x \leqslant 1, \quad (5)$$

where $\rho_0 = 1.0$, $\Delta\rho = 0.5$, $x_0 = 0.1$, $\Delta x = 0.1$.

Figure 1 shows a vertical cut through the 2D initial conditions for density, ρ, z-component of the magnetic field, B_z, and plasma flow velocity in x-direction, v_x. In Figure 1(a) we see an overlay of five different vertical cuts of the 2D density distribution at $y = 0$ ($\rho_{\mathrm{CH}} = 0.1$), $y = 0.25$ ($\rho_{\mathrm{CH}} = 0.2$), $y = 0.5$ ($\rho_{\mathrm{CH}} = 0.3$), $y = 0.75$ ($\rho_{\mathrm{CH}} = 0.4$), and $y = 1$ ($\rho_{\mathrm{CH}} = 0.5$). In the range $0.05 \leqslant x \leqslant 0.15$ we created a wave with the initial amplitude of $\rho = 1.5$ (for a detailed description see Equation (1)). We can see that the initial density amplitude of the incoming wave has the same value in all five cases, whereas the initial CH densities within the range $0.4 \leqslant x \leqslant 0.6$ vary from one vertical cut to another. The background density is equal to 1.0 everywhere. Figures 1(b) and (c) show the initial conditions for plasma flow velocity in x-direction, v_x, and z-component of the magnetic field, B_z. We can see that B_z and v_x are defined as functions of ρ in the range $0.05 \leqslant x \leqslant 0.15$. The initial amplitudes for v_x and B_z are the same for all cases of varying density distribution. The background magnetic field in the z-direction is equal to 1.0 over the whole computational box, whereas the magnetic field components in the x- and y-direction are equal to zero everywhere (see Equations (3) and (4)). The background plasma flow velocity in the x-direction is equal to zero and the plasma flow velocities for the y- and z-directions are equal to zero over the whole computational grid.

In Figure 2 we see the 2D initial conditions for the density distribution, showing a linearly increasing density from $\rho_{\mathrm{CH}} = 0.1$ up to $\rho_{\mathrm{CH}} = 0.5$ in the range $0.4 \leqslant x \leqslant 0.6$. The initial density amplitude of the incoming wave has the same value along the whole y-axis. This initial 2D setup enables us to perform simulations of the wave propagation for different CH

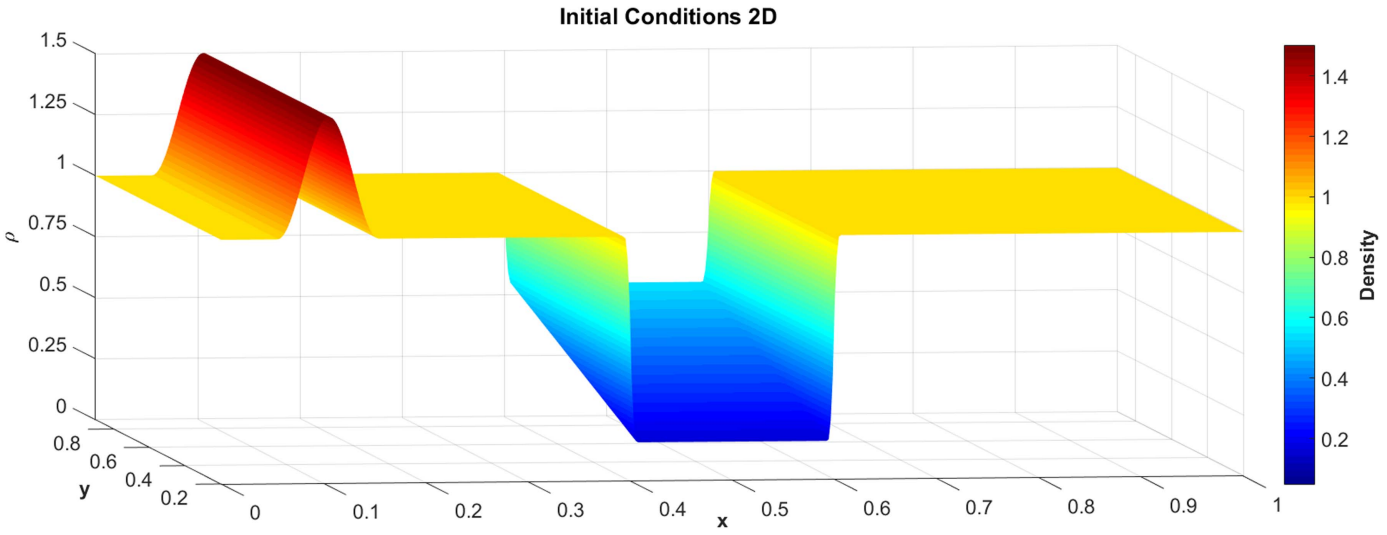

Figure 2. Initial 2D density distribution, showing a fixed initial wave amplitude of $\rho = 1.5$ and a linearly increasing CH density from $\rho_{CH} = 0.1$ up to $\rho_{CH} = 0.5$ in the range $0.4 \leqslant x \leqslant 0.6$. The background density is equal to 1.

densities simultaneously. Hence, the differences of phase speed and amplitude values due to varying densities inside the CH can be compared immediately.

3. Morphology

In Figures 3 and 4 we have plotted the temporal evolution of the density distribution for five different CH densities, starting at the beginning of the simulation run at $t = 0$ and ending at $t = 0.5$. We can see overlaid vertical cuts through the xz-plane of our simulations at $y = 0$, $y = 0.25$, $y = 0.5$, $y = 0.75$, and $y = 1$ at 10 different time steps. We observe the temporal evolution of the incoming wave (hereafter named primary wave) and its interaction with the CHs of different density values. Moreover, we can see the different behavior of the reflected, transmitted, and traversing waves (hereafter named secondary waves) due to varying density values inside the CH. We observe different kinds of stationary effects at the left CH boundary and also density depletions of varying depths, moving in the negative x-direction. In addition to that, we find that the primary wave is able to push the left CH boundary in the direction of the primary wave's propagation.

3.1. Primary Wave

In Figures 3(a) and (b), we can see how the primary wave is moving in the positive x-direction toward the left CH boundary. At the same time when the density amplitude starts decreasing, we observe a broadening of the width of the wave that is accompanied by a steepening of the wave and a subsequent shock formation.

3.2. Secondary Waves

After the primary wave has reached the left CH boundary (see Figure 3(c)), we find that the density amplitude quickly decreases when the wave starts traversing through the CH. The smallest density amplitude inside the CH can be seen for the case of an initial CH density of $\rho_{CH} = 0.1$ (blue), whereas the largest wave amplitude is observed in the case of $\rho_{CH} = 0.5$ (black). Furthermore, we observe immediate responses of the primary wave's impact on the left CH boundary (see Figures 3(c) and (d)). First, one can see a stationary feature that appears as a stationary peak at $x \approx 0.4$ in Figures 3(c)–(e) and 4(a). The morphology of this stationary feature will be discussed in Section 3.3. Second, we observe a first reflective feature (seen at $x \approx 0.37$ in Figures 3(c) and (d)), which is not able to move onward in the negative x-direction until the incoming wave has not completed the entry phase into the CH. Figures 3(e) and 4(a)–(d) show how this first reflection is finally moving toward the negative x-direction, where it is then difficult to distinguish from the background density. The first reflection is the same in all five cases of varying initial density inside the CH, and it is located on the left side of the density depletions. The smaller the initial density value inside the CH, the smaller the minimum value of the density depletion, i.e., the stronger the density depletion.

In Figures 3(c)–(e) one can see how the waves are traversing through the CH with much lower density amplitude than that of the primary wave. We observe that the smaller the initial density value inside the CH, the smaller the density amplitude of the traversing wave and the faster the wave propagates through the CH. For a better comparison of the different traversing waves we zoom in on the region $0.4 \leqslant x \leqslant 0.6$ in Figures 5–7. We choose the time interval from $t = 0.22481$ to $t = 0.47487$, which is the time interval where the traversing waves are moving back and forth inside the CH. Figure 5 shows that the waves are moving with approximately constant density amplitudes of $\rho = 0.11$ (for $\rho_{CH} = 0.1$), $\rho = 0.25$ (for $\rho_{CH} = 0.2$), $\rho = 0.39$ (for $\rho_{CH} = 0.3$), $\rho = 0.52$ (for $\rho_{CH} = 0.4$), and $\rho = 0.65$ (for $\rho_{CH} = 0.5$) toward the right CH boundary inside the CH. We saw in Figure 4 that at the time when the traversing waves reach the right CH boundary, one part of each wave is leaving the CH and is propagating onward as a transmitted wave. In Figure 6 we find that another part of the traversing waves gets reflected at the right CH boundary inside the CH. When these second traversing waves, which are propagating in the negative x-direction now, reach the left CH boundary, again one part leaves the CH hole, and this causes another stationary feature at the CH boundary outside of the CH (seen as sharp peaks in Figures 4(b)–(d)); this will be discussed in Section 3.3. Every one of these stationary features is followed by a wave that is moving in the negative x-direction (second reflection) while the stationary

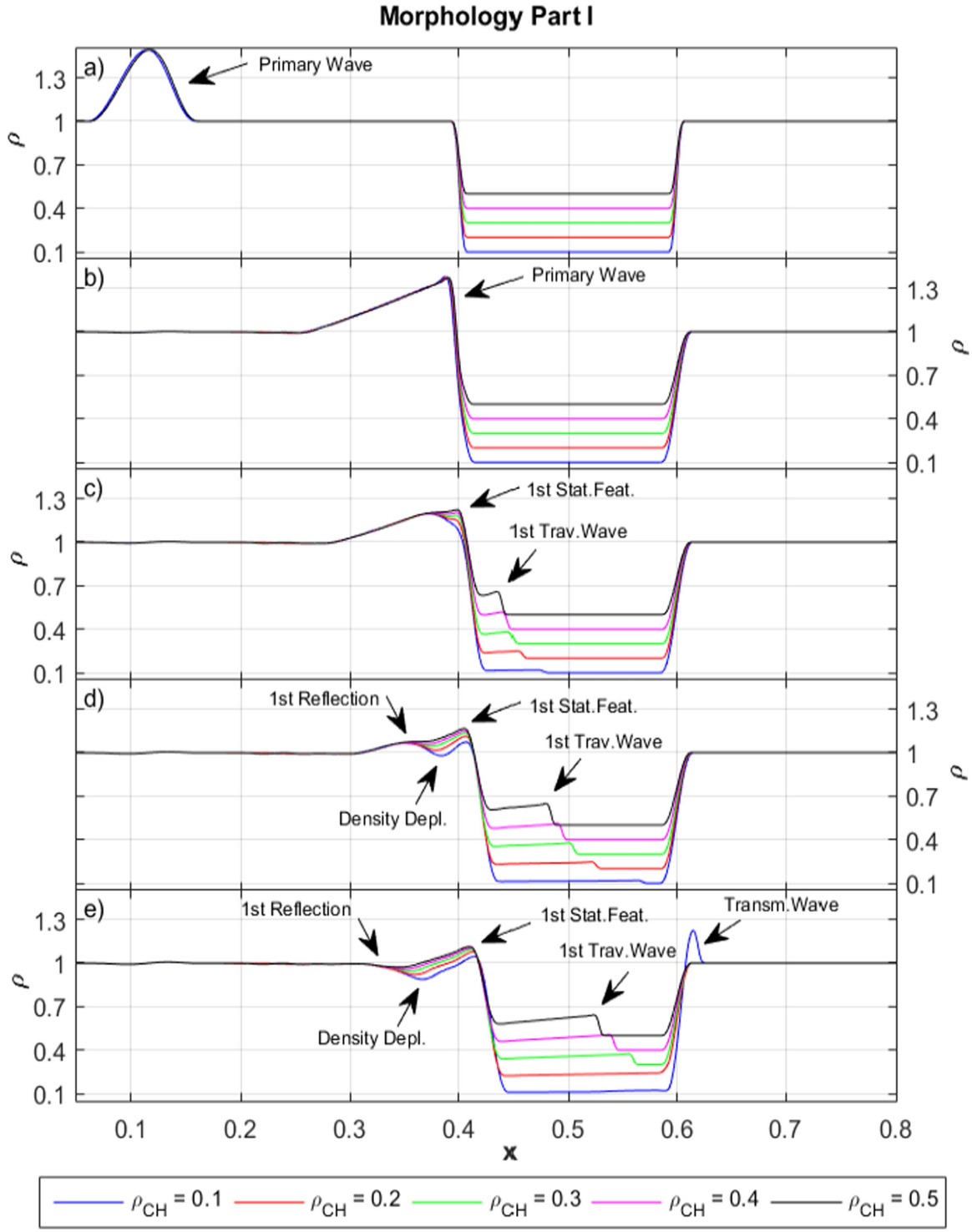

Figure 3. Overlay of the temporal evolution of the density distribution for all five different CH densities, starting at the beginning of the simulation run at $t = 0$ (panel (a)) and ending when the first transmitted wave occurs at $x \approx 0.6$ (blue line in panel (e)). The arrows denote the position of the primary wave, the first reflection, the first stationary feature, and the first traversing wave (for the case $\rho_{CH} = 0.5$; black) as well as the density depletion and the transmitted wave (for the case $\rho_{CH} = 0.1$; blue). (An animation of this figure is available.)

features can still be observed. The density amplitudes of this second reflection do not have a clear correlation with the initial density values inside the CH. A detailed analysis of the parameters of the second reflection will be performed in Section 4.2.

Due to the varying phase speeds inside the CH, the traversing waves leave the CH at different times. Hence, the smaller the density value inside the CH, the earlier we can observe the transmitted wave propagating outside of the CH. After leaving the CH, all different transmitted waves

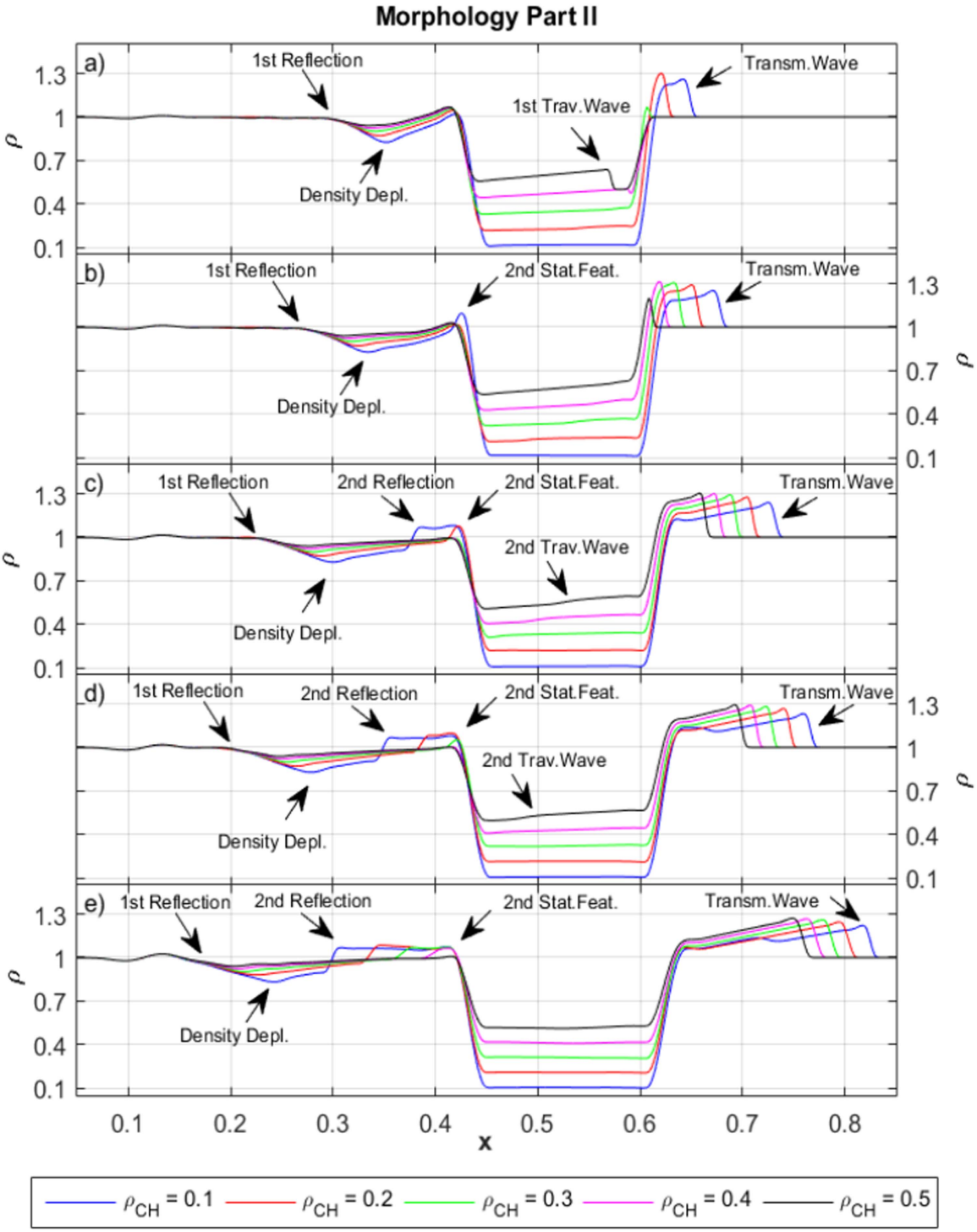

Figure 4. Continuation of Figure 3. Overlay of the temporal evolution of the density distribution for all five different CH densities, starting when the second transmitted wave occurs at $x \approx 0.6$ in panel (a) (red peak) and ending at the end of the simulation run at $t = 0.5$ (panel (e)). The arrows denote the position of the first reflection and the first and second traversing waves (for the case $\rho_{CH} = 0.5$; black), as well as the position for the density depletion, the second reflection, and the transmitted wave (for the case $\rho_{CH} = 0.1$; blue). The first occurrence of the second stationary feature is shown in the cases of four different CH densities (blue, red, green, and magenta) in panels (b)–(e).

keep moving onward in the positive x-direction until the end of the simulation run at $t = 0.5$ (see Figures 4(a)–(e)). One can see that the smaller the initial density inside the CH, the smaller the density amplitude of the transmitted wave (smallest density amplitude for the transmitted wave in the case of $\rho_{CH} = 0.1$, marked in blue; largest density amplitude for the transmitted wave in the case of $\rho_{CH} = 0.5$, marked in black).

Besides causing a second reflection, the second traversing waves get reflected inside the CH again and move a third time through the CH, again in the positive x-direction (see Figure 7). When this third traversing wave reaches the right CH

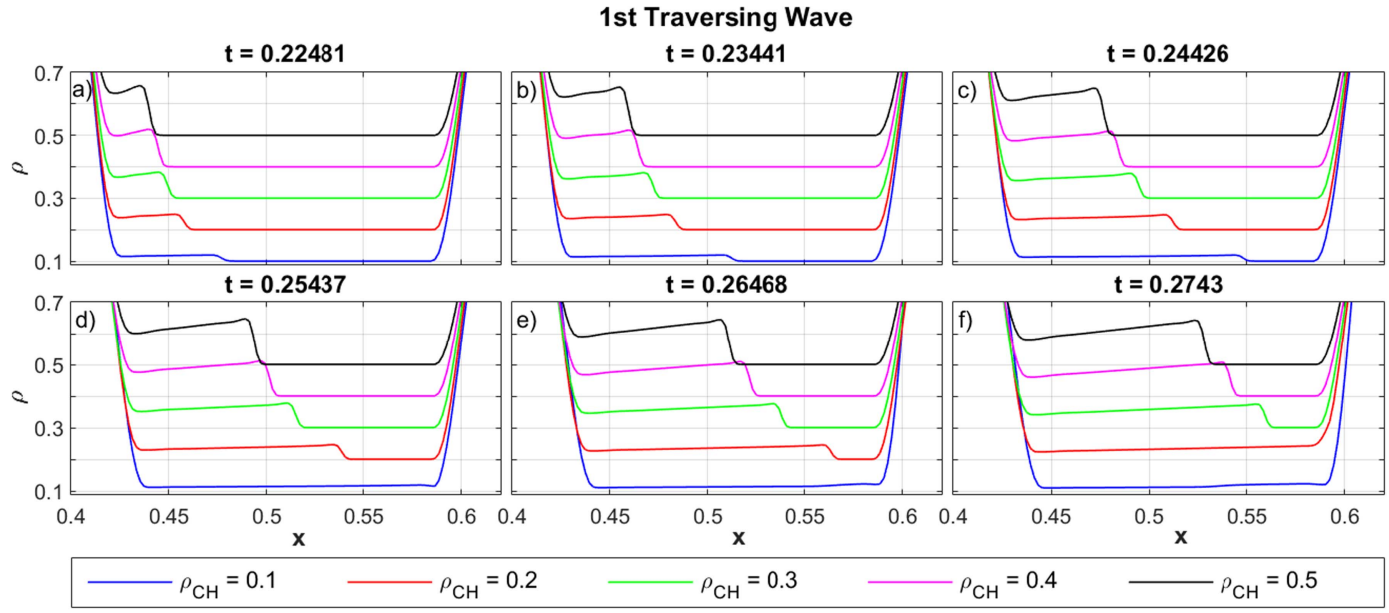

Figure 5. Temporal evolution of the density distribution of the first traversing wave moving in the positive x-direction inside the CH, starting shortly after the primary wave has entered the CH ($t = 0.22481$) and ending before one part of the wave with the smallest amplitude (blue) gets reflected inside the CH ($t = 0.2743$).

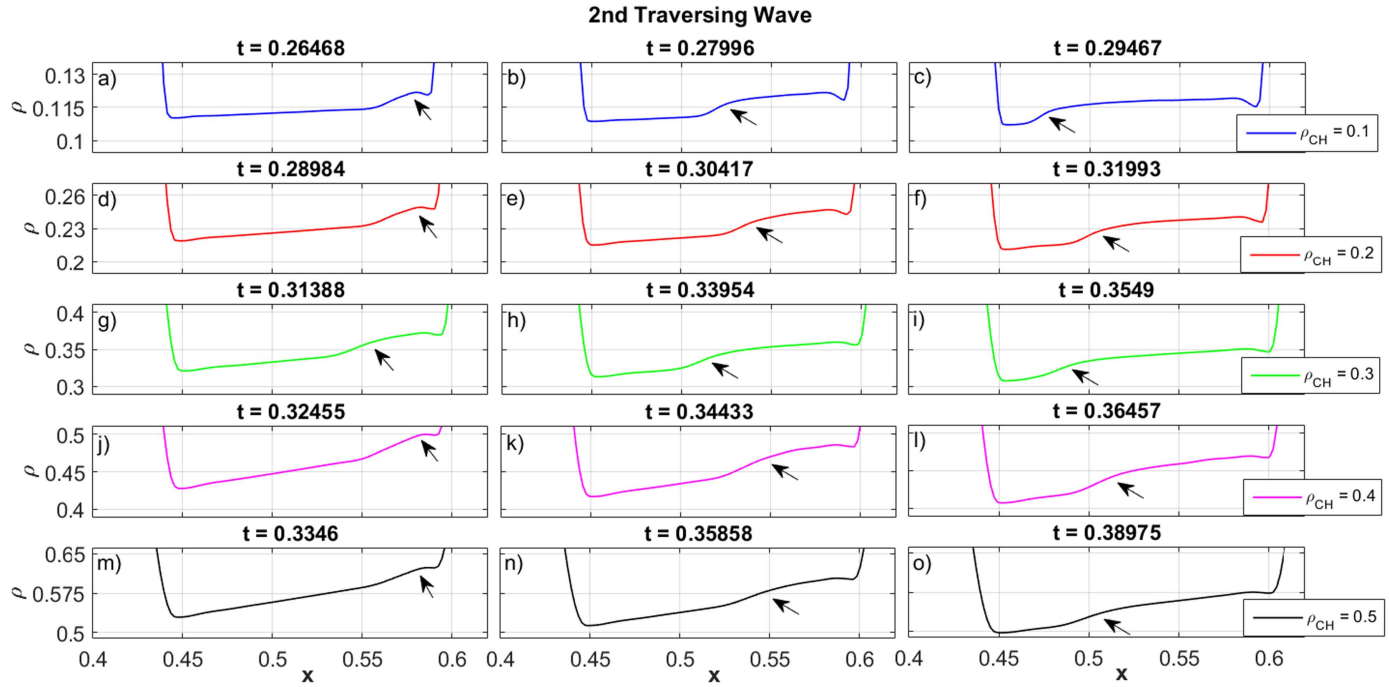

Figure 6. Temporal evolution of the density distribution of the second traversing wave moving in the negative x-direction inside the CH, starting shortly after the first traversing wave with the lowest amplitude (blue) got reflected at the right CH boundary inside the CH at $t = 0.26468$ and ending before the second traversing wave with the largest amplitude (black) reaches the left CH boundary inside the CH ($t = 0.38975$). The arrows denote the wave crest of the second traversing wave for all cases of different CH density.

boundary, it causes a kind of subwave inside the first transmitted wave, seen as a peak inside the already-existing transmitted wave in Figure 7. Since we cannot see these additional peaks inside the transmitted waves very clearly in Figure 7, we zoom in on the area of $0.6 < x < 0.9$. Figure 8 shows these peaks at $x \approx 0.76$ (for $\rho_{\rm CH} = 0.1$) and at $x \approx 0.685$ (for $\rho_{\rm CH} = 0.2$). This kind of second transmission moves together with the first transmission in the positive x-direction until the end of the simulation run at $t = 0.5$, but it can only be seen in the cases of $\rho_{\rm CH} = 0.1$ (blue) and $\rho_{\rm CH} = 0.2$ (red).

3.3. Stationary Features

We observe a first stationary feature at the left CH boundary; this appears as a stationary peak at $x \approx 0.4$ in Figures 3(c)–(e) and 4(a). This peak occurs in all five cases of different initial CH density, but it can be seen most clearly for the case of

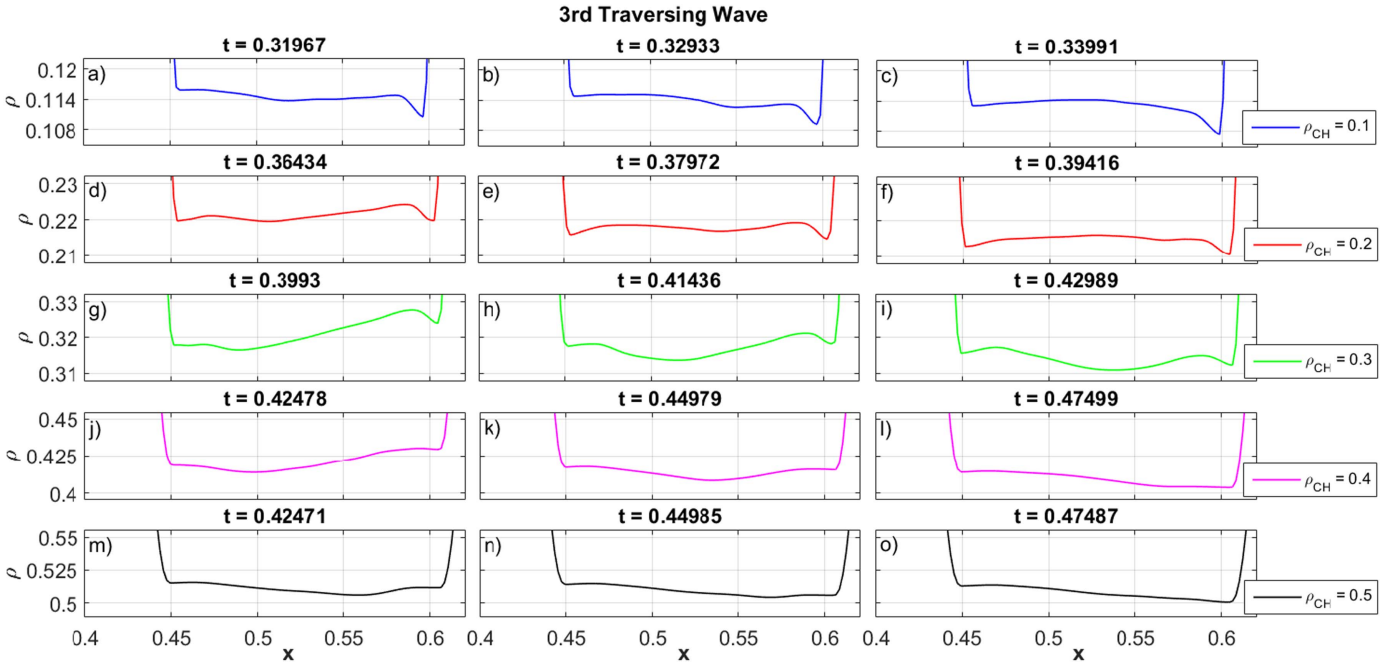

Figure 7. Temporal evolution of the density distribution of the third traversing wave moving in the positive x-direction inside the CH, starting shortly after the second traversing wave with the lowest amplitude (blue) got reflected at the left CH boundary inside the CH at $t = 0.31967$ and ending before the third traversing wave with the largest amplitude (black) reaches the right CH boundary inside the CH ($t = 0.47487$).

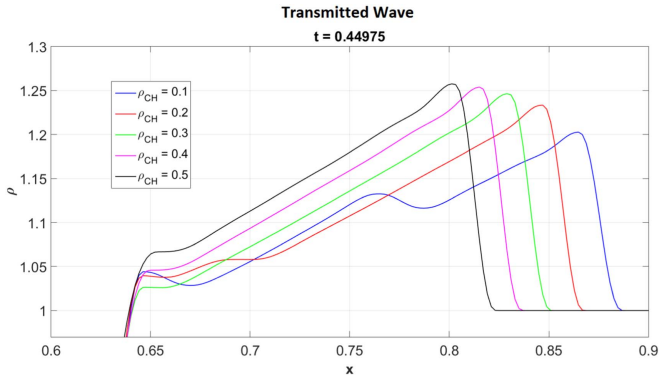

Figure 8. Zoom-in of the area of the transmitted waves in the range $0.6 \leqslant x \leqslant 0.9$ for the cases $\rho_{\rm CH} = 0.1$ (blue), $\rho_{\rm CH} = 0.2$ (red), $\rho_{\rm CH} = 0.3$ (green), $\rho_{\rm CH} = 0.4$ (magenta), and $\rho_{\rm CH} = 0.5$ (black).

$\rho_{\rm CH} = 0.5$ (black line). During the lifetime of these stationary features, the rear part of the primary wave continues to enter the CH and the traversing waves keep moving onward inside the CH. Due to the plot resolution on the one hand and the time delay of this feature for the different cases of $\rho_{\rm CH}$ on the other hand, the single peaks are hard to distinguish and detect in Figures 3(c) and (d). Hence, we zoom in on the area $0.3 \leqslant x \leqslant 0.5$ for the time period in which this first stationary feature occurs, in order to be able to study the peak values and the lifetime of this feature for all cases of different initial density inside the CH. Figure 9 shows that a stationary peak can be observed first in the case of $\rho_{\rm CH} = 0.1$ (blue line) at $x \approx 0.4$, followed by the peaks in the cases $\rho_{\rm CH} = 0.2$, $\rho_{\rm CH} = 0.3$, $\rho_{\rm CH} = 0.4$, and $\rho_{\rm CH} = 0.5$. The density of all peak values decreases in time, starting from $t = 0.22481$ and ending at $t = 0.29467$. One can see that the smaller the initial density inside the CH, the larger the peak value of this first stationary feature. Moreover, we can observe that the peak values move slightly in the positive x-direction for all different values of $\rho_{\rm CH}$.

In Figures 4(b)–(d) we find a second stationary feature at the left CH boundary at about $x \approx 0.43$. It occurs first for the case of $\rho_{\rm CH} = 0.1$ (blue), followed by the cases $\rho_{\rm CH} = 0.2$ (red), $\rho_{\rm CH} = 0.3$ (green), $\rho_{\rm CH} = 0.4$ (magenta), and $\rho_{\rm CH} = 0.5$ (black). In order to study the lifetime and the density peak values in detail, we zoom in on the region $0.3 \leqslant x \leqslant 0.5$ between $t = 0.31488$ and $t = 0.44975$. In contrast to the first stationary feature, Figure 10 shows that the smaller the initial density inside the CH, the larger the peak value of the second stationary feature. When we compare the time when the peaks show up with the time evolution of the traversing wave inside the CH, we see that the second stationary features appear at the time when the second traversing waves have reached the left CH boundary inside the CH again. We also find that the smaller the initial $\rho_{\rm CH}$ inside the CH is, the longer the lifetime of the second stationary peak. The peaks of this feature remain observable, while the second reflection is moving onward in the negative x-direction (see Figures 4(c)–(e)).

3.4. Density Depletion

In Figure 3(d) we observe the beginning of the evolution of a density depletion at $t \approx 0.39$, most clearly seen for the case $\rho_{\rm CH} = 0.1$ (blue) and located on the left side of the first stationary feature. This density depletion appears for all values of $\rho_{\rm CH}$ but has different minimum values. It propagates in the negative x-direction, ahead of the second reflection. One can see that the smaller the value for $\rho_{\rm CH}$, the smaller is the minimum value of the density depletion. One more time we zoom in on the area of interest ($0.2 \leqslant x \leqslant 0.4$) to analyze and compare the different depletions in detail. Figure 11 shows the time evolution of the density depletions from $t = 0.24967$ to $t = 0.39931$.

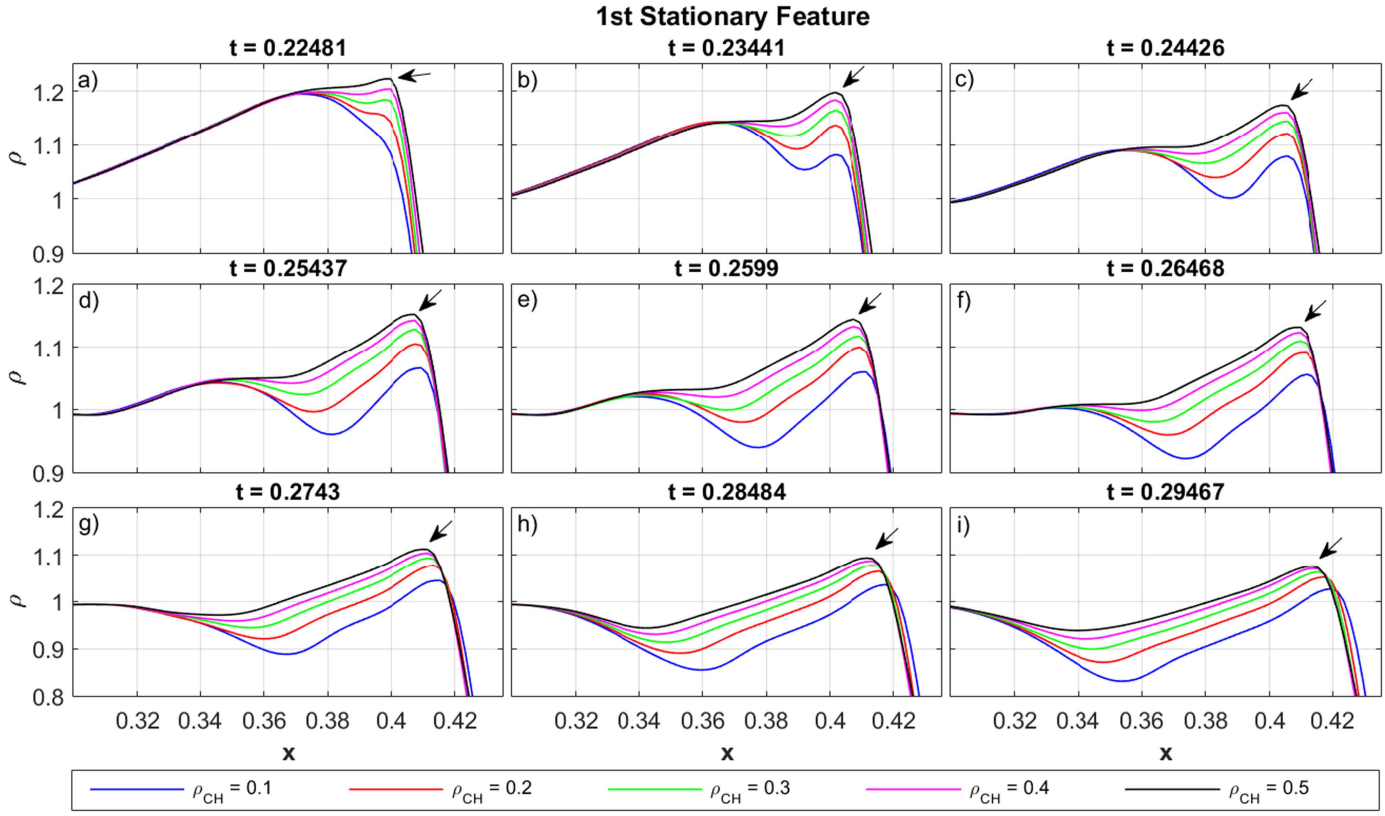

Figure 9. Zoom-in of the area of the first stationary feature in the range $0.3 \leqslant x \leqslant 0.44$ for the cases $\rho_{\rm CH} = 0.1$ (blue), $\rho_{\rm CH} = 0.2$ (red), $\rho_{\rm CH} = 0.3$ (green), $\rho_{\rm CH} = 0.4$ (magenta), and $\rho_{\rm CH} = 0.5$ (black), starting at $t = 0.22481$ and ending at $t = 0.29467$. The arrows denote the position of the peak value of the first stationary feature for the case $\rho_{\rm CH} = 0.5$ (black).

3.5. 2D Morphology

In Figure 12 we see the 2D temporal evolution of the density distribution for all cases of varying $\rho_{\rm CH}$, starting at $y = 0$ with $\rho_{\rm CH} = 0.1$ and increasing linearly to $\rho_{\rm CH} = 0.5$ at $y = 1$. Figure 12(a) shows the initial setup of the simulation run at $t = 0$. In Figure 12(b) one can see the primary wave shortly before the entry phase into the CH. What we observe in Figures 12(c) and (d) is how the wave enters the CH and starts traversing through the CH. We find that the smaller the value of $\rho_{\rm CH}$, the faster the wave traverses through the CH. Figure 12(e) shows that those waves that crossed a CH of low density already left the CH, while those that have entered a CH of a higher density value are still traversing through the CH. In Figure 12(f) we see that the second stationary feature starts appearing at the left CH boundary, caused by the first traversing waves reaching the left CH boundary. Moreover, in Figures 12(g)–(i) we can observe the evolution of the second stationary features for all cases of different $\rho_{\rm CH}$, as well as the propagation of the density depletion and the second reflection in the negative x-direction. How the transmissive waves for all different values for $\rho_{\rm CH}$ are moving forward in the positive x-direction can be seen in Figures 12(e)–(i).

Figure 13 shows the temporal evolution of the density amplitude and its position for the traversing and the transmitted waves in two different cases of CH density ($\rho_{\rm CH} = 0.1$ marked in blue and $\rho_{\rm CH} = 0.3$ marked in red) with regard to a wave having no interaction with a CH (gray). Furthermore, we compare the final density distribution for $\rho_{\rm CH} = 0.1$ (blue) and $\rho_{\rm CH} = 0.3$ (red) at the end of the simulation run at $t = 0.5$. One can see that the waves propagate faster through the CH ($0.4 \leqslant x \leqslant 0.6$) than the primary wave before entering the CH (gray for $0 < t < 0.2$). Moreover, we can observe how the density amplitudes decrease when the wave is traversing through the CH and how they increase again after having left the CH. By comparing the density amplitudes inside the CH, we can see that the amplitude value is much smaller for the case $\rho_{\rm CH} = 0.1$ (blue) than in the case $\rho_{\rm CH} = 0.3$ (red).

4. Kinematics

4.1. Primary Wave

Figure 14 shows the temporal evolution for the peak values of the primary wave's density, ρ, plasma flow velocity, v_x, phase speed, v_w, and magnetic field in the z-direction, B_z. In Figure 14(a) we find that the density amplitude stays approximately constant at a value of $\rho \approx 1.5$ until about $t = 0.06$ and decreases subsequently to a density value of $\rho \approx 1.4$ at $t = 0.2$, the time at which the primary wave starts entering the CH. A similar decrease can be seen in Figures 14(d) and (f), where we observe the plasma flow velocity and magnetic field component in the z-direction decreasing from $v_x \approx 0.45$, $B_z \approx 1.5$ at $t = 0.05$ to $v_x \approx 0.35$, $B_z \approx 1.4$ at $t = 0.2$. At the same time when the amplitude values of ρ, v_x, and B_z start decreasing, we observe a broadening of the width of the wave, starting at $\text{width}_{\rm wave} = 0.08$ ($t = 0$) and increasing to a value of $\text{width}_{\rm wave} = 0.13$ ($t = 0.2$) (see Figure 14(c)). Figure 14(b) shows how the wave is propagating in the positive x-direction. In Figure 14(e) it is evident that the phase speed of the primary wave decreases

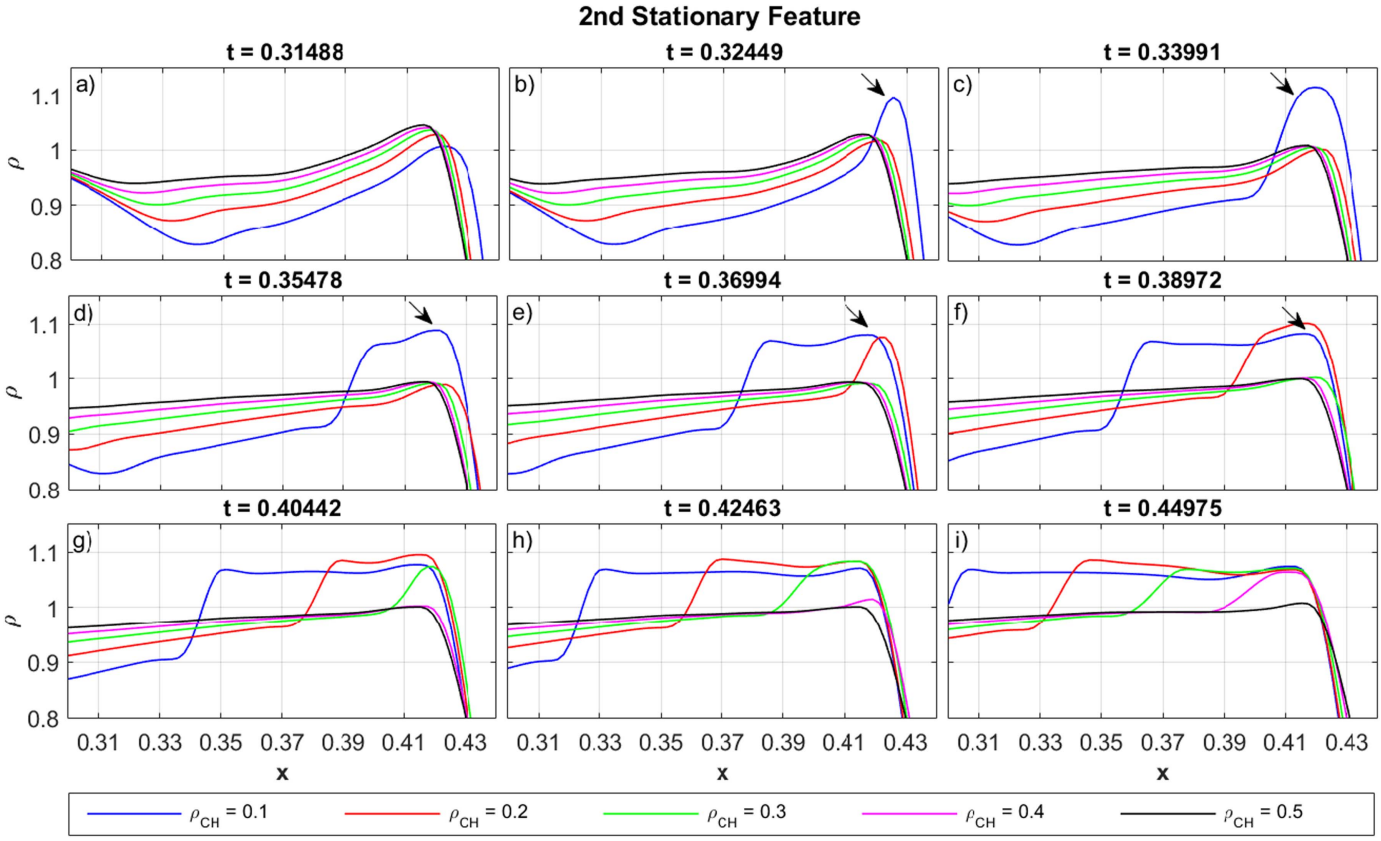

Figure 10. Zoom-in of the area of the second stationary feature in the range $0.3 \leqslant x \leqslant 0.44$ for the cases $\rho_{\rm CH} = 0.1$ (blue), $\rho_{\rm CH} = 0.2$ (red), $\rho_{\rm CH} = 0.3$ (green), $\rho_{\rm CH} = 0.4$ (magenta), and $\rho_{\rm CH} = 0.5$ (black), starting at $t = 0.31488$ and ending at $t = 0.44975$. The arrows denote the position of the peak value of the second stationary feature for the case $\rho_{\rm CH} = 0.1$ (blue).

slightly until the beginning of the entry phase into the CH, i.e., $v_w = 1.75$ (at $t = 0.01$) decreases to $v_w = 1.4$ (at $t = 0.2$).

4.2. Secondary Waves

Figure 15 shows the temporal evolution of density, ρ, position of the amplitude, Pos_A, plasma flow velocity, v_x, phase speed, v_w, and magnetic field component in the z-direction, B_z, for the first traversing wave in every case of varying CH density, $\rho_{m\mathrm{CH}}$. In all five cases the wave is propagating with approximately constant amplitude in the positive x-direction (see Figures 15(a) and (b)), i.e., $\rho = 0.11$ (for $\rho_{\rm CH} = 0.1$; blue), $\rho = 0.25$ (for $\rho_{\rm CH} = 0.2$; red), $\rho = 0.39$ (for $\rho_{\rm CH} = 0.3$; green), $\rho = 0.52$ (for $\rho_{\rm CH} = 0.4$; magenta), and $\rho = 0.65$ (for $\rho_{\rm CH} = 0.5$; black). Figure 15(e) shows the values for the magnetic field component in the z-direction. One can see that, like in the case of the density ρ, the amplitudes remain approximately constant and that the smaller the CH density, $\rho_{\rm CH}$, the smaller the amplitude value of B_z. The tracking of the wave with $\rho_{\rm CH} = 0.5$ starts at a later time owing to the different phase speeds of the traversing waves inside the CH. In Figure 15(c) we observe approximately constant values for v_x, but in contrast to the density, ρ, and the magnetic field component in z-direction, B_z, the largest amplitudes can be seen in the case of $\rho_{\rm CH} = 0.1$ and the smallest ones for $\rho_{\rm CH} = 0.5$. The temporal evolution of the phase speed of the first traversing wave is shown in Figure 15(d). We find that the smaller the intial density inside the CH, the faster the wave propagates through the CH. In all five cases the phase speed decreases slightly until the wave leaves the CH, i.e., at $t = 0.215$ we have $v_w \approx 3.75$ (for $\rho_{\rm CH} = 0.1$), $v_w \approx 2.5$ (for $\rho_{\rm CH} = 0.2$), $v_w \approx 2.15$ (for $\rho_{\rm CH} = 0.3$), and $v_w \approx 1.75$ (for $\rho_{\rm CH} = 0.4$). The speed tracking in the case of $\rho_{\rm CH} = 0.5$ starts at $t \approx 0.222$ and supplies a value of $v_w \approx 1.7$. The phase speed values decrease until $t = 0.24$ to $v_w \approx 3.2$ (for $\rho_{\rm CH} = 0.1$), $v_w \approx 1.9$ (for $\rho_{\rm CH} = 0.2$), $v_w \approx 1.9$ (for $\rho_{\rm CH} = 0.3$), $v_w \approx 1.5$ (for $\rho_{\rm CH} = 0.4$), and $v_w \approx 1.25$ (for $\rho_{\rm CH} = 0.5$). (Due to the very low amplitudes inside the CH on the one hand and the related tracking difficulties on the other hand, there will be no detailed kinematics study of the second and third traversing waves.)

The temporal evolution of the parameters of the transmitted waves is described in Figure 16. In Figures 16(a), (b), and (e), where one can see the amplitude values of ρ, v_x, and B_z, it is evident that the wave that was traversing through the CH in the case $\rho_{\rm CH} = 0.1$ (blue line) leaves the CH first, followed by the waves in the cases of $\rho_{\rm CH} = 0.2$ (red), $\rho_{\rm CH} = 0.3$ (green), $\rho_{\rm CH} = 0.4$ (magenta), and $\rho_{\rm CH} = 0.5$ (black). The density amplitude values of the transmitted waves start at $\rho = 1.27$ (for $\rho_{\rm CH} = 0.1$ at $t \approx 0.28$), $\rho = 1.3$ (for $\rho_{\rm CH} = 0.2$ at $t \approx 0.3$), $\rho = 1.32$ (for $\rho_{\rm CH} = 0.3$ at $t \approx 0.32$), $\rho = 1.325$ (for $\rho_{\rm CH} = 0.4$ at $t \approx 0.33$), and $\rho = 1.325$ (for $\rho_{\rm CH} = 0.5$ at $t \approx 0.337$) and decrease to $\rho = 1.24$ (for $\rho_{\rm CH} = 0.1$), $\rho = 1.28$ (for $\rho_{\rm CH} = 0.2$), $\rho = 1.29$ (for $\rho_{\rm CH} = 0.3$), $\rho = 1.3$ (for $\rho_{\rm CH} = 0.4$), and $\rho = 1.305$ (for $\rho_{\rm CH} = 0.5$) at the end of the simulation run at $t = 0.5$ (see Figure 16(a)). Figure 16(c) shows how the transmitted waves propagate in the positive x-direction in all five cases. The evolution of the phase speed of the transmitted waves is described in Figure 16(d). Here we can see that the values start at $v_w = 1.21$ (for $\rho_{\rm CH} = 0.1$), $v_w = 1.18$ (for $\rho_{\rm CH} = 0.2$), $v_w = 1.17$ (for $\rho_{\rm CH} = 0.3$),

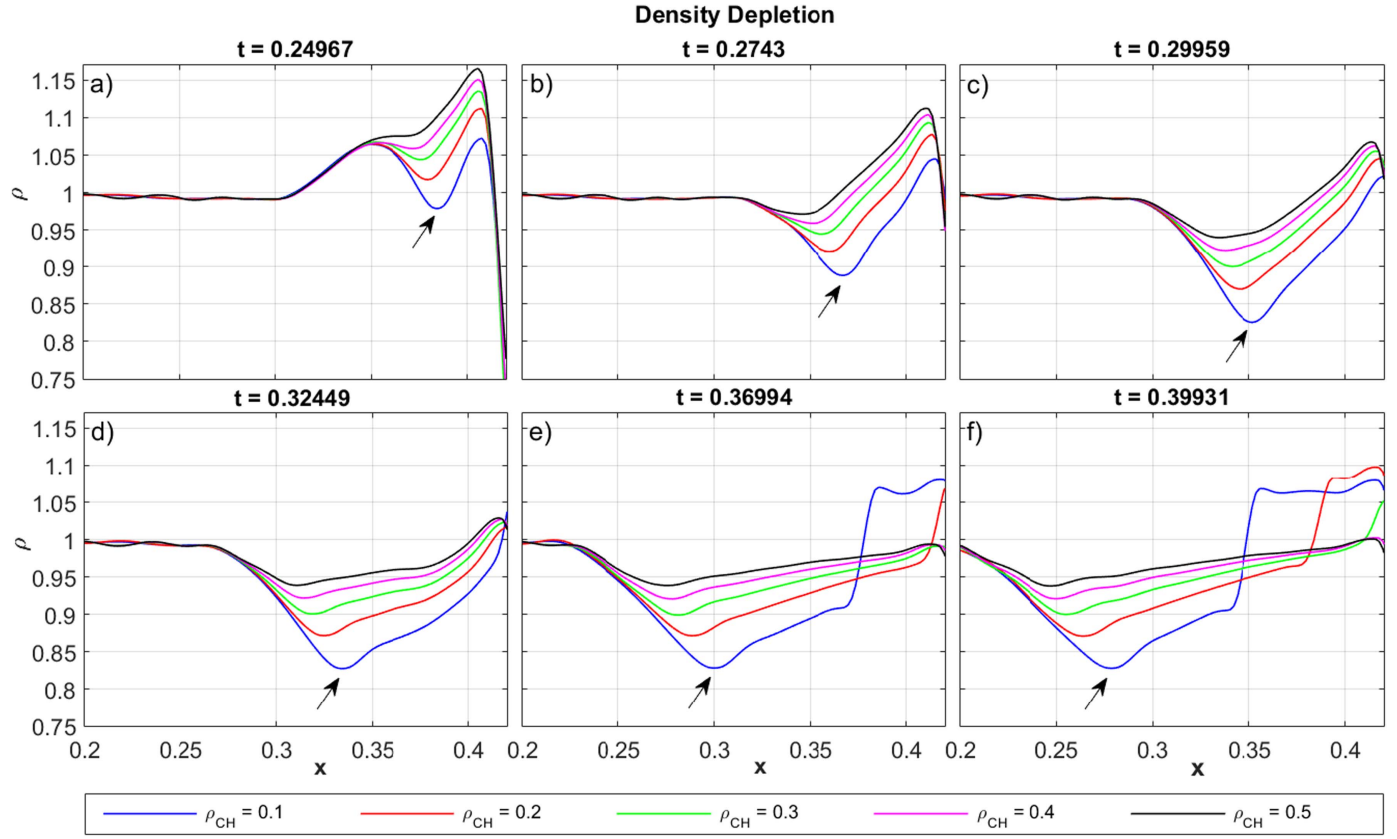

Figure 11. Zoom-in of the area of the density depletion ahead of the first reflection in the range $0.2 \leqslant x \leqslant 0.42$ for the cases $\rho_{CH} = 0.1$ (blue), $\rho_{CH} = 0.2$ (red), $\rho_{CH} = 0.3$ (green), $\rho_{CH} = 0.4$ (magenta), and $\rho_{CH} = 0.5$ (black). The arrows denote the position of the minimum value of the density depletion for the case $\rho_{CH} = 0.1$ (blue).

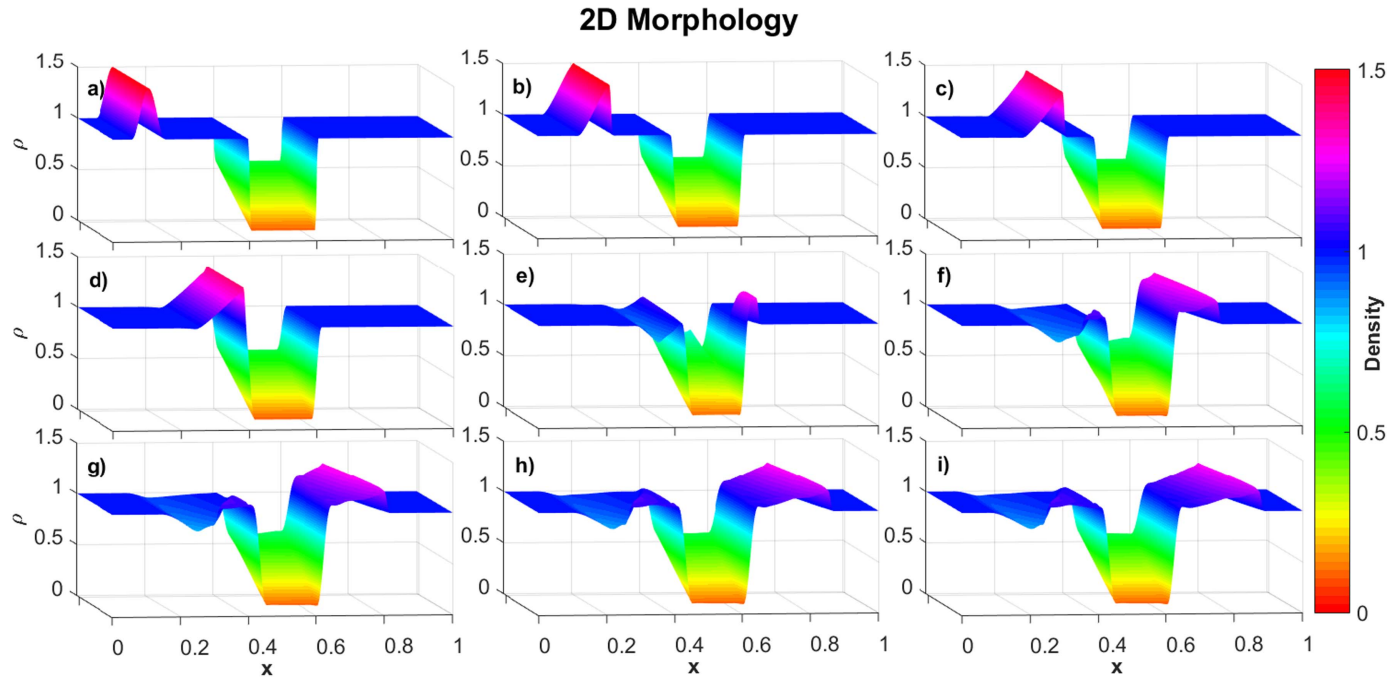

Figure 12. Temporal evolution of density distribution for all different CH densities at the same time, starting at the beginning of the simulation run at $t = 0$ and ending at $t = 0.5$.

$v_w = 1.17$ (for $\rho_{CH} = 0.4$), and $v_w = 1.17$ (for $\rho_{CH} = 0.5$) and decrease slightly in all five cases as the wave is moving further toward the positive x-direction.

Figure 17 describes the amplitude values of the first reflection. Due to a superposition, caused by a simultaneous entering of segments of the rear of the primary wave into the

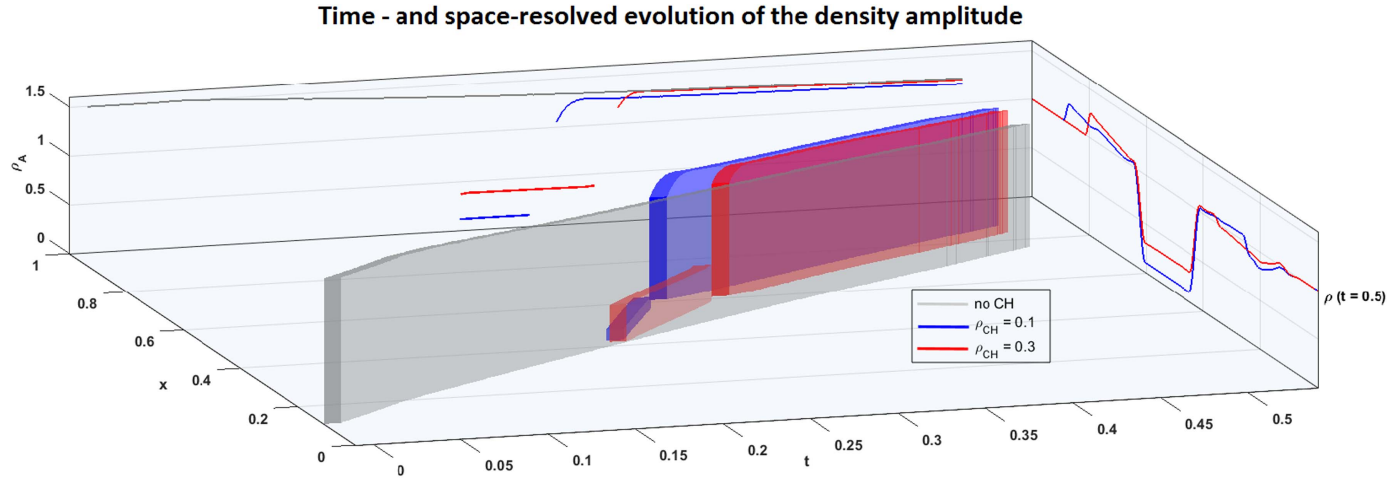

Figure 13. The 3D plot in the center of the figure shows the temporal evolution of the amplitude position and the density amplitude ρ_A for the cases $\rho_{CH} = 0.1$ (blue) and $\rho_{CH} = 0.3$ (red). The plot in the back compares the density amplitudes of the traversing wave and the transmitted wave for the cases $\rho_{CH} = 0.1$ (blue) and $\rho_{CH} = 0.3$ (red) with regard to the density amplitude of a wave with no interaction with a CH (gray). The plot on the right compares the density distribution at the end of the simulation run ($t = 0.5$) for the cases $\rho_{CH} = 0.1$ (blue) and $\rho_{CH} = 0.3$ (red).

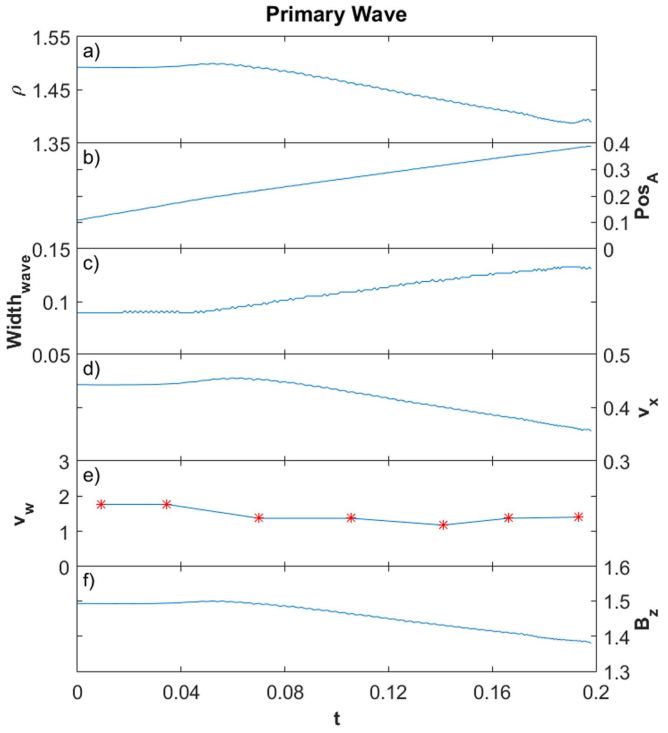

Figure 14. From top to bottom: density, position of the amplitude, width of the wave, plasma flow velocity, phase velocity, and magnetic field of the primary wave, from the beginning of the run ($t = 0$) until the time when the wave is entering the CH ($t = 0.2$).

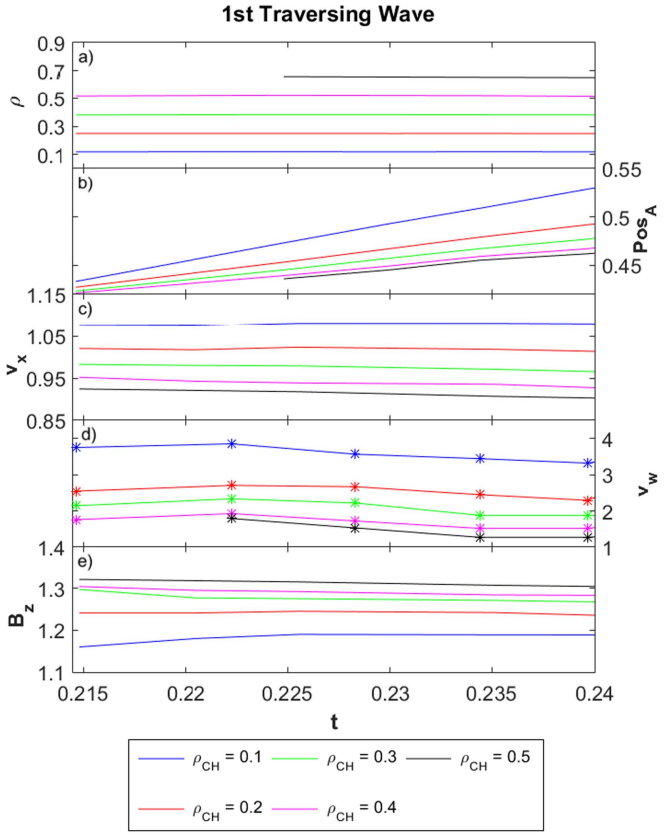

Figure 15. From top to bottom: temporal evolution of density, position of the amplitude, plasma flow velocity, phase velocity, and magnetic field of the traversing wave for the cases $\rho_{CH} = 0.1$ (blue), $\rho_{CH} = 0.2$ (red), $\rho_{CH} = 0.3$ (green), $\rho_{CH} = 0.4$ (magenta), and $\rho_{CH} = 0.5$ (black), starting at about $t = 0.215$, shortly after the primary wave has entered the CH, and ending at $t = 0.24$, when the traversing waves leave the CH.

CH on the one hand and an already ongoing reflection of the front segments of the wave on the other hand, this feature is not able to move in the negative x-direction until the primary wave has completed its entry phase into the CH. Hence, we will start describing the kinematics of this first reflection at $t \approx 0.27$, when it starts moving in the negative x-direction.

As we can see in Figures 4(a)–(e), the first reflection is the same in all cases of different ρ_{CH}. It moves from $x \approx 0.3$ (seen in Figure 4(a)) to $x \approx 0.2$ (seen in Figure 4(d)) and is located on the left side of the density depletions. Figure 17 describes the kinematics of this first reflection for all different ρ_{CH}. In Figure 17(a) one can see that the amplitude density stays at an approximately constant value of about $\rho = 1.0$ until $t \approx 0.39$. At that time the first reflection approaches an area of oscillations that is caused by numerical effects (detailed description in Piantschitsch et al. 2017). Here we can no longer get reasonable results for the first reflection. Similar to

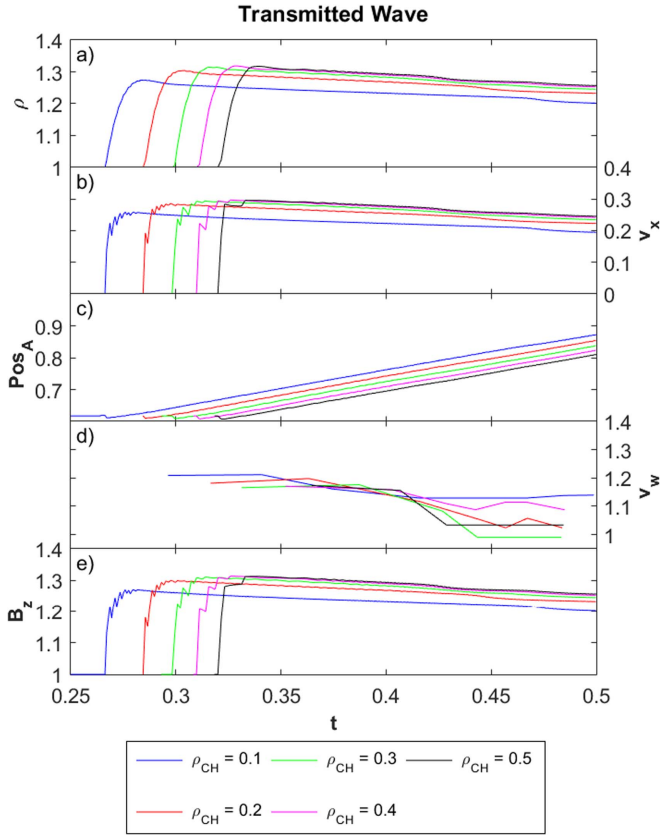

Figure 16. From top to bottom: temporal evolution of density, plasma flow velocity, position of the amplitude, phase velocity, and magnetic field of the transmitted wave for the cases $\rho_{CH} = 0.1$ (blue), $\rho_{CH} = 0.2$ (red), $\rho_{CH} = 0.3$ (green), $\rho_{CH} = 0.4$ (magenta), and $\rho_{CH} = 0.5$ (black), starting at about $t = 0.26$, when the first transmitted wave (blue) occurs at the right CH boundary, and ending at the end of the simulation run at $t = 0.5$.

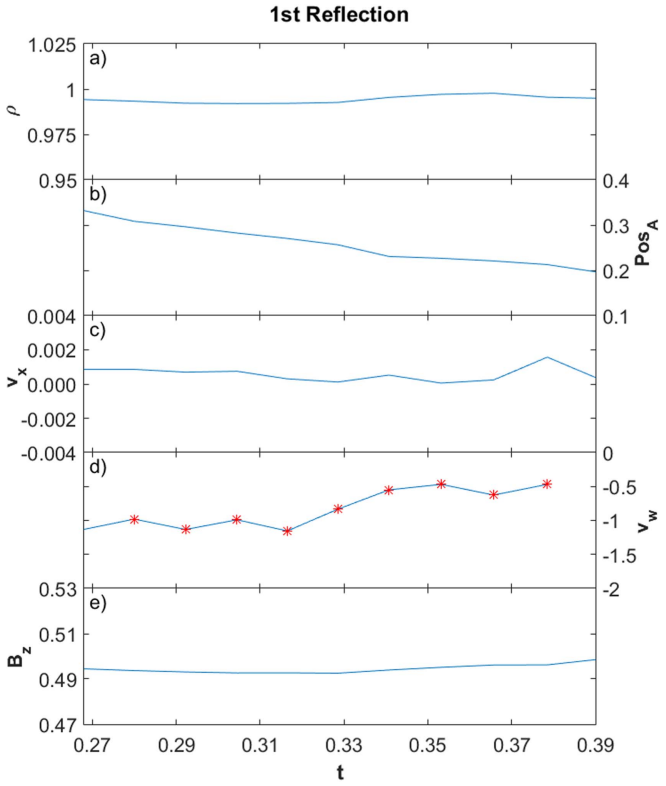

Figure 17. From top to bottom: temporal evolution of density, position of the amplitude, plasma flow velocity, phase velocity, and magnetic field of the first reflection, starting at $t \approx 0.27$ and ending at $t = 0.39$.

the density values of this first reflection, the magnetic field component, B_z, and plasma flow velocity, v_x, stay approximately constant at values of $B_z = 0.495$ or $v_x = 0.001$ (see Figures 17(c) and (e)). Figure 17(b) shows how the reflection is moving in the negative x-direction. The temporal evolution of the phase speed of this first reflection is described in Figure 17(d). Here we observe that the value of the phase speed decreases from $v_w \approx -1.1$ to $v_w \approx -0.5$.

In Figure 18 we present the kinematic analysis of the second reflection. This reflection is caused by parts of the traversing wave leaving the CH at the left CH boundary at $t \approx 0.36$. At the time at which we stop the simulation run, $t = 0.5$, only the reflections for the cases $\rho_{CH} = 0.1$, $\rho_{CH} = 0.2$, and $\rho_{CH} = 0.3$ have moved sufficiently far in the negative x-direction to compare their peak values. Figure 18 shows how the time at which the second reflection appears depends on the density inside the CH. In contrast to traversing and transmitted waves, we do not have a linear correlation between the initial density values inside the CH and the amplitude values of the different reflection parameters. Figure 18(a) shows that the density amplitude for the case $\rho_{CH} = 0.2$ (red) is in fact larger than the density amplitude in the case $\rho_{CH} = 0.1$ (blue). However, the density amplitude in the case $\rho_{CH} = 0.3$ (green) is not larger than the one in the case $\rho_{CH} = 0.2$ (red) but lies between the first two cases. A similar behavior holds true for the plasma flow velocity, v_x, and the magnetic field component, B_z (see Figures 18(b) and (d)). In Figure 18(c) one can see how the second reflection is moving in the negative x-direction until the end of the simulation run at $t = 0.5$.

4.3. Stationary Features

The kinematics of the first stationary feature are described in Figure 19. In Figure 19(a) we can see that at about $t \approx 0.22$ this feature occurs first in the case of $\rho_{CH} = 0.5$ (black), starting with a density amplitude of $\rho \approx 1.25$ and decreasing to $\rho \approx 1.0$ at $t = 0.36$. This density plot also shows that the appearances of the other density amplitudes follow one after each other: $\rho = 1.23$ (for $\rho_{CH} = 0.4$, magenta, at $t = 0.22$), $\rho = 1.2$ (for $\rho_{CH} = 0.3$, green, at $t = 0.225$), $\rho = 1.18$ (for $\rho_{CH} = 0.2$, red, at $t = 0.23$), and $\rho = 1.16$ (for $\rho_{CH} = 0.1$, blue, at $t = 0.229$). Finally, these amplitude values decrease to $\rho \approx 1.0$ (in all five cases of different ρ_{CH}). A similar decreasing behavior can be observed for the magnetic field component in the z-direction, B_z (see Figure 19(e)). The amplitude values of B_z start at approximately the same values as the density amplitudes in Figure 19(a) and decrease also to a value of $B_z = 1.0$ at $t = 0.36$. Figures 19(a) and (e) show that the smaller the density inside the CH, the larger the wave's amplitude values for density and magnetic field. The exact reverse behavior can be observed for the plasma flow velocity, v_x, and phase speed, v_w, of this feature (see Figures 19(b) and (d)). Here it is evident that the smaller the density value inside the CH, the smaller the values for v_x and v_w. Figure 19(c) shows that the first stationary feature is moving slightly in the positive x-direction in all five cases of different ρ_{CH}.

In Figure 20 we present the kinematic analysis of the second stationary feature. Figures 20(a) and (e) show, in contrast to the first stationary feature, that the smaller the initial density inside

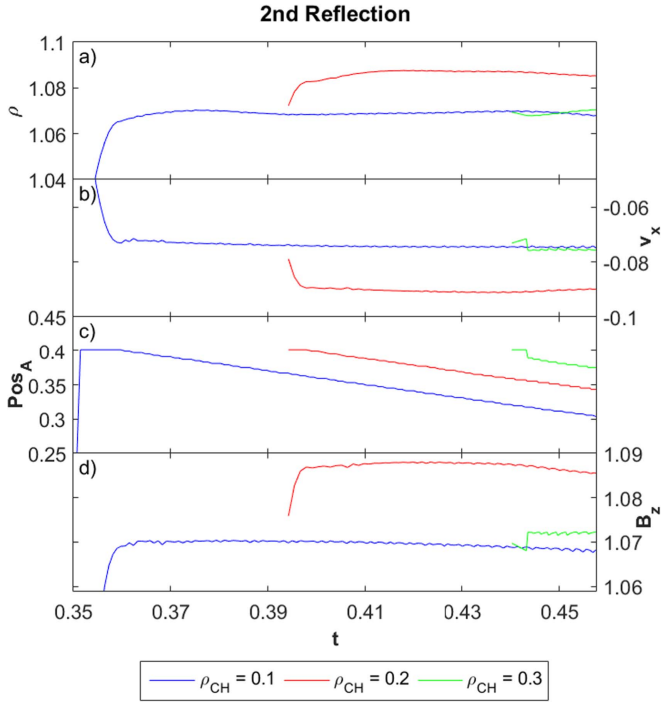

Figure 18. From top to bottom: temporal evolution of density, plasma flow velocity, position of the amplitude, and magnetic field of the second reflection for the cases $\rho_{CH} = 0.1$ (blue), $\rho_{CH} = 0.2$ (red), and $\rho_{CH} = 0.3$ (green), starting at about $t = 0.35$, when the second reflection occurs for the case $\rho_{CH} = 0.1$ (blue), and ending at the end of the simulation run, $t = 0.5$.

the CH, ρ_{CH}, the larger the amplitude values for density, ρ, and magnetic field component, B_z. Another difference between the first and the second stationary features is the fact that the second stationary feature is moving slightly in the negative x-direction (see Figure 20(c)). Since the movement of this feature is more or less only a small shift of its position to the left, plasma flow velocity v_x and phase speed v_w are very small too and finally decrease to a value of almost zero in all five cases of different ρ_{CH} (see Figures 20(b) and (d)).

4.4. Density Depletion

In Figure 21 we analyze the temporal evolution of the density depletion for all different cases of initial CH density. This feature occurs first for the case $\rho_{CH} = 0.1$ (blue) at about $t = 0.25$, followed by the density depletions for $\rho_{CH} = 0.2$ (red), $\rho_{CH} = 0.3$ (green), $\rho_{CH} = 0.4$ (magenta), and $\rho_{CH} = 0.5$ (black). The minimum density values of the depletion decrease from about $\rho = 1.0$ (for all five cases) to $\rho = 0.83$ ($\rho_{CH} = 0.1$, blue), $\rho = 0.87$ ($\rho_{CH} = 0.2$, red), $\rho = 0.9$ ($\rho_{CH} = 0.3$, green), $\rho = 0.92$ ($\rho_{CH} = 0.4$, magenta), and $\rho = 0.94$ ($\rho_{CH} = 0.5$, black) at $t = 0.3$ and subsequently remain approximately constant at those values until the end of the run at $t = 0.5$ (see Figure 21(a)). An analogous behavior to the density evolution can be found for the temporal evolution of the magnetic field component B_z (see Figure 21(e)). In Figure 21(b) we find a decrease of the plasma flow velocity for all five cases of different intial CH density ρ_{CH}. At $t = 0.25$ we find a value of $v_x \approx 0.35$, which decreases down to $v_x \approx 0.17$ (at $t = 0.3$) in the case of $\rho_{CH} = 0.1$ (blue). A similar decrease can be found for all the other cases: the density values $v_x \approx 0.24$ (red, at $t \approx 0.258$), $v_x \approx 0.18$ (green, at $t \approx 0.26$), $v_x \approx 0.13$ (magenta, at $t \approx 0.268$), and $v_x \approx 0.08$ (black, at $t \approx 0.27$) decrease to

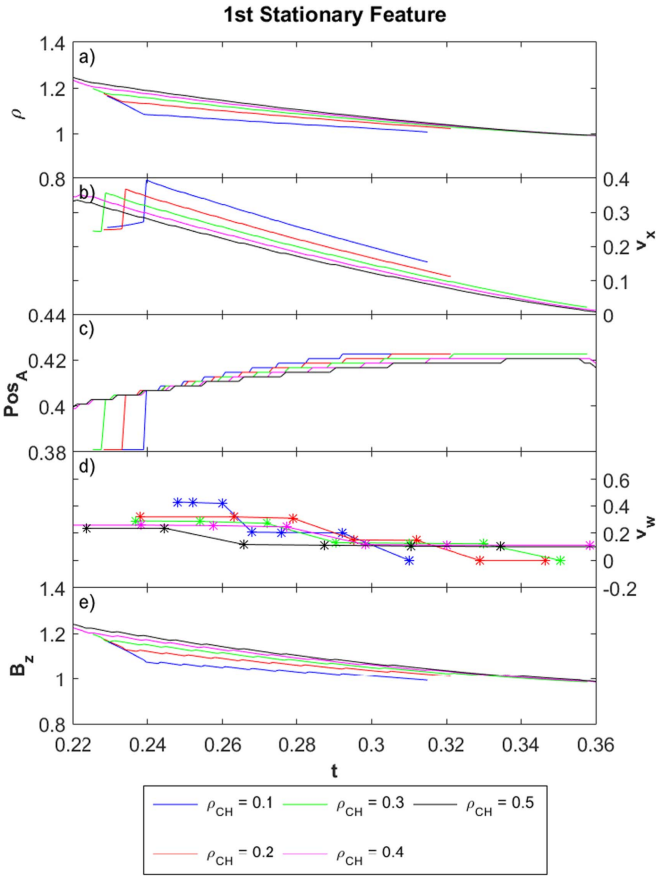

Figure 19. From top to bottom: temporal evolution of density, plasma flow velocity, position of the amplitude, phase velocity, and magnetic field of the first stationary feature for the cases $\rho_{CH} = 0.1$ (blue), $\rho_{CH} = 0.2$ (red), $\rho_{CH} = 0.3$ (green), $\rho_{CH} = 0.4$ (magenta), and $\rho_{CH} = 0.5$ (black), starting at about $t = 0.22$, when this feature occurs first in the case of $\rho_{CH} = 0.5$ (black), and ending at $t \approx 0.36$.

$v_x \approx 0.13$ (red), $v_x \approx 0.1$ (green), $v_x \approx 0.07$ (magenta), and $v_x \approx 0.05$ (black) and then remain at those values until $t = 0.5$. Figure 21(c) shows how all density depletions are moving toward the negative x-direction. Furthermore, we observe that the smaller the density inside the CH, the smaller the mean phase speed of the density depletion (see Figure 21(d)).

5. Discussion

In Piantschitsch et al. (2017) we showed that the impact of the incoming fast-mode MHD wave on the CH leads to effects like reflection, transmission, and the formation of stationary fronts. In this paper we focus on how the CH density influences all these different features. We find that the CH density correlates with the peak values of the stationary features and the amplitudes of the secondary waves.

When we compare the first reflection and the first stationary feature with each other, we see that both effects are connected to a superposition of wave parts that are entering the CH and wave parts that were already reflected at the CH boundary. In detail, this means that segments of the rear of the primary wave are entering the CH while segments of the front of the primary wave have already been reflected at the left CH boundary but are prevented from moving in the negative x-direction owing to the plasma flow associated with the primary wave. The significant difference between those two features is that the

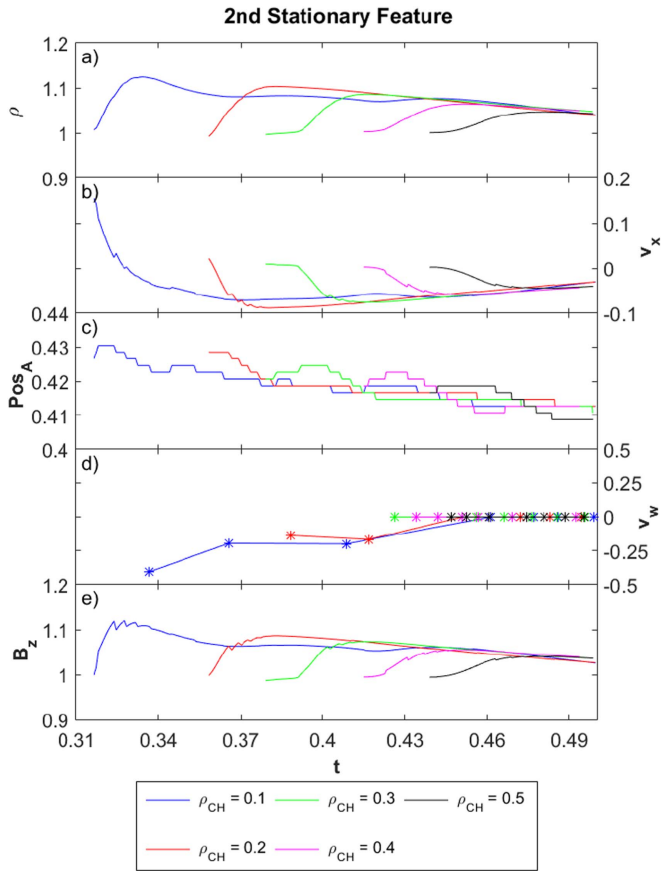

Figure 20. From top to bottom: temporal evolution of density, plasma flow velocity, position of the amplitude, phase velocity, and magnetic field of the second stationary feature for the cases $\rho_{CH} = 0.1$ (blue), $\rho_{CH} = 0.2$ (red), $\rho_{CH} = 0.3$ (green), $\rho_{CH} = 0.4$ (magenta), and $\rho_{CH} = 0.5$ (black), starting at about $t = 0.32$, when this feature occurs first in the case of $\rho_{CH} = 0.1$ (blue), and ending at the end of the simulation run, $t = 0.5$.

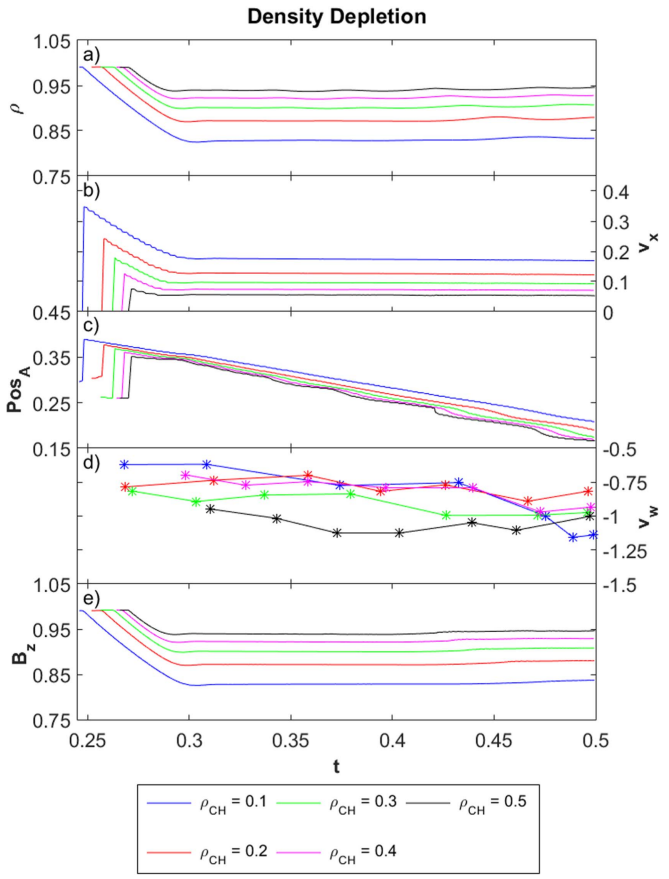

Figure 21. From top to bottom: temporal evolution of density, plasma flow velocity, position of the amplitude, phase velocity, and magnetic field of the density depletion for the cases $\rho_{CH} = 0.1$ (blue), $\rho_{CH} = 0.2$ (red), $\rho_{CH} = 0.3$ (green), $\rho_{CH} = 0.4$ (magenta), and $\rho_{CH} = 0.5$ (black), starting at about $t = 0.25$, when this feature occurs first in case of $\rho_{CH} = 0.1$ (blue) and ending at the end of the simulation run, $t = 0.5$.

first reflection is a moving feature and its parameters are the same for all five cases of different CH density. The first stationary feature, on the other hand, exhibits different amplitudes depending on the various CH densities. This means, further, that the first reflection is only caused by the immediate response of the primary's wave impact on the CH boundary. The first stationary feature, in contrast, seems to be also affected by the different CH densities.

A comparison between the first and second stationary features shows that these effects depend on the initial CH density in the opposite manner. The smaller the initial CH density is, the larger the amplitudes for the second stationary feature are. In contrast, the smaller the initial CH density is, the smaller the density amplitudes of the first stationary feature are. An explanation for this could be a combination of the effects of the traversing waves on the one hand and reflections inside the CH on the other hand in the case of the second stationary feature. We showed in the kinematics section that the smaller the initial CH density, the smaller the density amplitude of the traversing wave and the smaller the density amplitude of the transmitted wave. This consequently also means that in the case of low initial CH density a bigger part gets reflected inside the CH and leads finally to a larger peak value of the second stationary feature.

The second reflection exhibits notable properties since there is no linear correlation between its amplitudes and the initial CH density. This feature seems to be more complex since it combines effects of the traversing waves, their phase speed, and reflections inside the CH.

During the analysis of the transmitted waves, we found an additional peak inside the wave, a kind of subwave that is moving with the transmitted wave in the positive x-direction. This phenomenon only occurs for the cases of $\rho_{CH} = 0.1$ and $\rho_{CH} = 0.2$. A reason for this is probably the limited runtime of the simulation, i.e., we expect to see those peaks in the transmitted waves for the other three cases as well for a longer runtime of the simulation. We found that these peaks occur when the third traversing wave reaches the right CH boundary.

When considering our simulation results, we have to bear in mind that we are dealing with an idealized situation including many constraints, e.g., a homogeneous magnetic field, the fact that the pressure is equal to zero over the whole computational box, the assumption of a certain value for the initial wave amplitude, and a simplified shape of the CH. Another thing we have to pay attention to is the fact that in our simulations we assume a certain width of the CH. We do not know so far how much a broader CH would influence the final phase speed of the traversing waves and hence the properties of the transmitted waves, as well as the reflective features inside the CH.

In our simulations we observe a quite large density amplitude of the transmitted wave, whereas in observations such transmitted waves are rarely found. Only in Olmedo et al. (2012) was a wave for the first time reported being transmitted through a CH. Hence,

there are some aspects, such as the intensity of the wave's driver (solar flare or CME), the distance of the initial wave front to the CH, the shape and size of the CH, and the magnetic field structure inside the CH, that we have to keep in mind when comparing observations with our simulations. More specifically, in our simulations we make sure that the amplitude of the incoming wave is large enough and that the distance to the CH is sufficiently small in order to guarantee a transmission through the CH. In observations, due to a possibly weak eruption or a large distance of the wave's driver to the CH, this cannot be guaranteed. Another issue is the shape of the CH; in our simulations the wave is approaching exactly perpendicular to the CH at every point, whereas this is usually not the case in the observations. Moreover, the size of a CH can also be a reason for preventing a wave traversing through the whole CH. In our simulations we assume a homogeneous magnetic field, which does not reflect the actual magnetic field structure of a CH in the observations. The complexity of the magnetic field structure inside a CH may also be a cause for the wave not being transmitted through the CH, due to, e.g., dispersion of the wave on inhomogenities. We also have to be aware that our simulations are restricted to two dimensions, that is, the wave front is not capable of moving in the vertical direction as would be the case in the observations.

6. Conclusions

We present the results of a newly developed 2.5D MHD code performing simulations of a fast-mode MHD wave interacting with CHs of different density and various Alfvén speeds. In Piantschitsch et al. (2017) we demonstrated that the impact of the incoming wave causes different effects such as reflection, transmission, and the formation of stationary fronts for the case of an initial density amplitude of $\rho = 1.5$ and a fixed initial CH density of $\rho_{\rm CH} = 0.1$.

In this paper, we focus on comparing the properties of the different secondary waves and the stationary features with regard to various CH densities and different Alfvén speeds. We observe that the CH density is correlated to the amplitude values of the secondary waves and the peak values of the stationary features. The main simulation results look as follows:

1. For the first traversing wave we found that the smaller the initial CH density, the smaller the wave's density amplitude and magnetic field component in z-direction, and the larger the amplitudes for phase speed and plasma flow velocity (see Figures 5 and 15). The crucial point is that the different CH densities correspond to different Alfvén speeds inside the CH and hence to different phase speeds of the traversing waves.
2. The analysis of the transmitted waves showed that the smaller the initial CH density, the smaller the amplitudes for density, magnetic field component in the z-direction, and plasma flow velocity, and the larger the phase speed (see Figures 8 and 16).
3. We observe a very weak dependence of the first reflection on the CH density with regard to the initial parameters we choose for our simulations. The reflection seems to be mostly driven by the impact of the incoming wave on the CH boundary (see Figures 4 and 17).
4. The kinematic analysis of the second reflection has shown that we do not find a linear correlation between the initial CH density and the peak values for the different parameters of this feature as we have found for traversing and transmitted waves, as well as for both stationary features (see Figure 18).
5. For the first stationary feature we have demonstrated that the smaller the initial CH density, the smaller the peak values of density and of magnetic field component in the z-direction. The stationary feature is moving slightly in the positive x-direction (see Figures 9 and 19).
6. On the contrary, in the case of the second stationary feature we observe that the smaller the initial CH density, the larger the peak values of density and magnetic field component. This second stationary feature is moving slightly in the negative x-direction (see Figures 10 and 20).
7. By analyzing the kinematics of the density depletion, we found that the smaller the initial CH density, the smaller the minimum density values of the depletion. Moreover, we find that the smaller the density values inside the CH, the larger the values of plasma flow velocity and phase speed (see Figures 11 and 21).

As already shown in Piantschitsch et al. (2017), these findings strongly support the wave interpretation of large-scale disturbances in the corona. First, effects like reflection and transmission can only be explained by a wave theory. We do not know of any other mechanism that would explain reflection or transmission of coronal waves. Second, the simulation results show that the interaction of an MHD wave and a CH is capable of forming stationary features, which were one of the main reasons for the development of a pseudo-wave theory.

We compared our simulation results to observations in Kienreich et al. (2013), where the authors observed reflected features that consist of a bright lane followed by a dark lane in base-difference images. These observations correspond to the first reflection and the density depletion in our simulation.

The authors gratefully acknowledge the helpful comments from the anonymous referee that have very much improved the quality of this paper. This work was supported by the Austrian Science Fund (FWF): P23618 and P27765. B.V. acknowledges financial support by the Croatian Science Foundation under the project 6212 Solar and Stellar Variability. I.P. is grateful to Ewan C. Dickson for proofreading this manuscript. B.V. thanks the International Space Science Institute, Bern (ISSI) for the support and hospitality during his stay at ISSI as a member of teams D. Long & S. Bloomfield, "The Nature of Coronal Bright Fronts" and M. Luna, "Large—Amplitude Oscillations in Solar Prominences," during which many of the ideas presented in this work have been discussed. The authors gratefully acknowledge support from NAWI Graz.

ORCID iDs

Isabell Piantschitsch https://orcid.org/0000-0001-9124-6644
Bojan Vršnak https://orcid.org/0000-0002-0248-4681
Arnold Hanslmeier https://orcid.org/0000-0002-7282-5007
Birgit Lemmerer https://orcid.org/0000-0001-5199-770X
Astrid Veronig https://orcid.org/0000-0003-2073-002X
Jaša Čalogović https://orcid.org/0000-0002-4066-726X

References

Attrill, G. D. R., Harra, L. K., van Driel-Gesztelyi, L., & Démoulin, P. 2007a, ApJL, 656, L101
Attrill, G. D. R., Harra, L. K., van Driel-Gesztelyi, L., Démoulin, P., & Wülser, J.-P. 2007b, AN, 328, 760

Chandra, R., Chen, P. F., Fulara, A., Srivastava, A. K., & Uddin, W. 2016, ApJ, 822, 106
Chen, P. F., Fang, C., Chandra, R., & Srivastava, A. K. 2016, SoPh, 291, 3195
Chen, P. F., Fang, C., & Shibata, K. 2005, ApJ, 622, 1202
Chen, P. F., Wu, S. T., Shibata, K., & Fang, C. 2002, ApJL, 572, L99
Chen, P. F., & Wu, Y. 2011, ApJL, 732, L20
Cheng, X., Zhang, J., Olmedo, O., et al. 2012, ApJL, 745, L5
Cohen, O., Attrill, G. D. R., Manchester, W. B., IV, & Wills-Davey, M. J. 2009, ApJ, 705, 587
Delaboudinière, J.-P., Artzner, G. E., Brunaud, J., et al. 1995, SoPh, 162, 291
Delannée, C., Hochedez, J.-F., & Aulanier, G. 2007, A&A, 465, 603
Domingo, V., Fleck, B., & Poland, A. I. 1995, SoPh, 162, 1
Downs, C., Roussev, I. I., van der Holst, B., et al. 2011, ApJ, 728, 2
Gopalswamy, N., Yashiro, S., Temmer, M., et al. 2009, ApJL, 691, L123
Harra, L. K., Sterling, A. C., Gömöry, P., & Veronig, A. 2011, ApJL, 737, L4
Kienreich, I. W., Muhr, N., Veronig, A. M., et al. 2013, SoPh, 286, 201
Liu, W., Nitta, N. V., Schrijver, C. J., Title, A. M., & Tarbell, T. D. 2010, ApJL, 723, L53
Long, D. M., Bloomfield, D. S., Chen, P. F., et al. 2017, SoPh, 292, 7
Long, D. M., Gallagher, P. T., McAteer, R. T. J., & Bloomfield, D. S. 2008, ApJL, 680, L81
Lulić, S., Vršnak, B., Žic, T., et al. 2013, SoPh, 286, 509
Ofman, L., & Thompson, B. J. 2002, ApJ, 574, 440
Olmedo, O., Vourlidas, A., Zhang, J., & Cheng, X. 2012, ApJ, 756, 143
Patsourakos, S., & Vourlidas, A. 2009, ApJL, 700, L182
Patsourakos, S., Vourlidas, A., Wang, Y. M., Stenborg, G., & Thernisien, A. 2009, SoPh, 259, 49
Piantschitsch, I., Vršnak, B., Hanslmeier, A., et al. 2017, APJ, 850, 88
Schmidt, J. M., & Ofman, L. 2010, ApJ, 713, 1008
Thompson, B. J., Plunkett, S. P., Gurman, J. B., et al. 1998, GeoRL, 25, 2465
Tóth, G., & Odstrčil, D. 1996, JCoPh, 128, 82
van Driel-Gesztelyi, L., Attrill, G. D. R., Démoulin, P., Mandrini, C. H., & Harra, L. K. 2008, AnGeo, 26, 3077
Veronig, A. M., Gömöry, P., Kienreich, I. W., et al. 2011, ApJL, 743, L10
Veronig, A. M., Muhr, N., Kienreich, I. W., Temmer, M., & Vršnak, B. 2010, ApJL, 716, L57
Veronig, A. M., Temmer, M., & Vršnak, B. 2008, ApJL, 681, L113
Vršnak, B., & Cliver, E. W. 2008, SoPh, 253, 215
Vršnak, B., & Lulić, S. 2000, SoPh, 196, 157
Wang, Y.-M. 2000, ApJL, 543, L89
Warmuth, A. 2015, LRSP, 12, 3
Warmuth, A., Vršnak, B., Magdalenić, J., Hanslmeier, A., & Otruba, W. 2004, A&A, 418, 1101
Wu, S. T., Zheng, H., Wang, S., et al. 2001, JGR, 106, 25089
Zhukov, A. N., & Auchère, F. 2004, A&A, 427, 705
Zong, W., & Dai, Y. 2017, ApJL, 834, L15